Engineering of strong and hard *in-situ* Al-Al$_3$Ti nanocomposite via high-energy ball milling and spark plasma sintering

S. Vorotilo[a,*], A.A. Nepapushev[a], D.O. Moskovskikh[a], V.S. Buinevich[a], G.V. Trusov[a], D. Yu. Kovalev[b], A.O. Semenyuk[c], N.D. Stepanov[c], K. Vorotilo[a], A.Y. Nalivaiko[a], A.A. Gromov[a]

[a] *National University of Science and Technology MISiS, Moscow, Russia*
[b] *Merzhanov Institute of Structural Macrokinetics and Materials Science Russian Academy of Sciences, Chernogolovka, Russia*
[c] *Laboratory of Bulk Nanostructured Materials, Belgorod State University, Belgorod, Russia*

ARTICLE INFO

ABSTRACT

Light-weight Al-Ti nanocomposites attract increasing attention due to the advancements in spacecraft and additive manufacturing. In this work, a*b initio* modeling, DSC, and in-situ XRD experiments were used to formulate a strategy for rapid fabrication of Al-Al$_3$Ti nanocomposites with enhanced mechanical properties (ultimate tensile strength up to 437 MPa at room temperature and up to 109 MPa at 500 °C, ~6% elongation before failure), resulting from a mixed ductile-fragile deformation behavior. The investigated samples were produced by spark plasma sintering of high-energy ball-milled reactive composites Al-TiH$_2$ leading to the precipitation of 0.05–0.25 µm Al$_3$Ti particles from the nanostructured Al matrix. Samples with coarser TiH$_2$ powder or higher TiH$_2$ content featured a minor amount of transitional core-shell structures resulting from the incomplete conversion of the as-formed Ti particles into Al$_3$Ti. The following phase and structure formation mechanism upon the heating of the reactive nanocomposite powders was proposed: $Al + \delta\ TiH_2 \xrightarrow{\sim 450-500°C} Al[Ti] + \beta\ Ti[Al] + \delta\ TiH_{2-x} \xrightarrow{\sim 550-600°C} Al + Al_3Ti$. Tentative guidelines for the sintering of Al-TiH$_2$ composites were proposed based on the analysis of diffusion kinetics.

© 2021 Published by Elsevier B.V.

1. Introduction

Aluminum-based metal matrix composites (Al-MMCs) have high electrical/thermal conductivity and specific strength due to their low density [1]. Due to these enhanced properties, Al-MMCs are intended to replace many monolithic materials for structural and multi-functional applications [2]. In particular, the combination of density (ρ = 2.7 – 3.0 g/cm^3), strength (200–400 MPa), and relatively low production costs [3] makes Al-MMCs attractive for aerospace and automotive industries.

Various additives have been used to enhance the mechanical properties of Al-MMCs: Al$_2$O$_3$ [4], TiB$_2$ [5], TiC [6,7], SiC [8], and BN [9]; carbon nanotubes [10,11], intermetallics and metallic glasses [12–15]. Reinforcing phases have been introduced into the aluminum matrix by *in-situ* and *ex-situ* approaches; for *in-situ* approaches, the reinforcing phase is formed during processing, for example during casting [16] or thermal treatment [17]. *Ex-situ* approaches use additives that are chemically inert during processing

with composite formed by solid-phase and liquid-phase consolidation of the powder mixtures: the addition of reinforcing particles into the Al melt, impregnation of ceramic frameworks using Al, etc [18–20]. Considering this, *in-situ* approaches generally result in better adhesion between the reinforcing phases and matrix due to the formation of coherent phase boundaries within the system [21]. Additionally, the *in-situ* formed phases have higher wettability, are more thermodynamically stable, and have fewer impurities on their surface [21].

Aluminides are an effective reinforcing phase for Al matrixes due to their high specific strength at room temperature and under heating. Specifically, the high melting point (1340 °C), low density (3.4 g/cm^3), and high Young's modulus (216 GPa) [22] make Al$_3$Ti an excellent reinforcement phase for Al-MMC. One of the simplest and most convenient ways to produce *in-situ* reinforcements is the reaction between Ti or Ti-containing compounds (e.g. K$_2$TiF$_6$) with the Al matrix during casting [21,23–26]. However, it is difficult to control the grain size of the reinforcing phase, leading to reduced mechanical properties of the composite. Powder metallurgical techniques allow for more control over the composition and grain size of the composites. In particular, the grains size can be tuned by the application of various low- and high-intensity milling procedures and

by thermal or thermo-mechanical treatment. A recent study of Al-Al$_3$Ti composite produced by high energy vibromilling with subsequent hot extrusion [27–29] showed that 4 h milling of the reactive mixture resulted in the formation of nanosized aluminum particles (63 nm), mechanochemical synthesis of minor amounts of Al$_3$Ti, and that hot extrusion increased the Al$_3$Ti content [27]. Milling aluminum powder is difficult due to the inherent plasticity of aluminum; during mechanical treatment, Al powders experience intense plastic deformation and form elongated Al microsheets, which strongly adhere to milling jar and grinding media. To facilitate milling, a surface-active process control agent (PCA) is added (usually stearic acid (CH$_3$(CH$_2$)$_{16}$COOH). The PCA adsorbs to the surface of Al particles, decreasing the surface free energy of the Al particles, minimizing the formation of large agglomerates [30]. Since most PCAs are organic, contamination of the material by residual oxygen and carbon can emerge upon sintering, thus embrittling the composite. On the other hand, controlled, reversible hydrogen-driven embrittlement can be instrumental in decreasing the grain size of the composite powders.

In this work, we produce Al/Al$_3$Ti composites by an *in-situ* approach using high-energy ball milling (HEBM) [31,32] of the precursor mixture with subsequent Spark Plasma Sintering (SPS) [33,34]. TiH$_2$ was used in conjunction with Al powder to minimize adherence to the milling media during HEBM, and form uniform, submicron composite particles during milling [32]. Moreover, TiH$_2$ has a relatively low decomposition temperature (400–750 °C) and releases hydrogen upon decomposition, leading to reduction of surface oxides and grain refinement of the composite particles, resulting in better consolidation [35]. The combination of HEBM and SPS reduces the overall fabrication time: HEBM reduces the powder mixture treatment duration, while SPS provides faster sintering rates and stimulates TiH$_2$ decomposition [33,36]. The main focus of this study is the investigation of the influence of the TiH$_2$ content and HEBM duration on the microstructure and mechanical properties of the Al/Al$_3$Ti *in-situ* composite, in addition to the exploration of the relevant phase formation mechanisms.

2. Materials and methods

2.1. Construction of grand potential phase diagrams

For the estimation of phase stability, we employed AFLOW-CHULL: Cloud-Oriented Platform for Autonomous Phase Stability Analysis [37] as well as Materials Project Phase Diagram App and Interface Reactions App [38–40]. AFLOW-Chull and Materials Project employ databases of DFT computed bulk material energies with crystal structures obtained from the Inorganic Crystal Structure Database (ICSD) [41] and data-mined chemical substitutions [42–44]. We used the 0.1 eV/atom energy above the convex hull as the phase metastability threshold after [45].

In grand potential phase diagrams, the chemical potential (μ) represents the effect of temperature and partial pressure of the particular element (in our case, hydrogen). More negative values correspond to higher temperatures and lower partial pressures [46]. Grand potential phase diagrams represent the behavior of complex hydrogen-containing systems with reasonable accuracy [38,39,44].

2.2. Experimental

The following powders were used as precursors: (I) Al (ASD-6 grade, Russia) with a purity of > 99% and a particle size within 10 μm, (II) titanium hydride (Plazmoterm, Russia) with a purity of 99.5% and an average particle size of 12 μm. Stearic acid was used as a PCA.

Table 1
Sample abbreviation, composition, and milling regimes used in the work.

Sample's abbreviation	Composition	Milling regime
1TiH$_2$	Al + 1 wt% TiH$_2$	5 min of TiH$_2$ pre-milling + 10 min milling
1.5TiH$_2$	Al + 1.5 wt% TiH$_2$	
5TiH$_2$	Al + 5 wt% TiH$_2$	
10TiH$_2$	Al + 10 wt% TiH$_2$	
15TiH$_2$	Al + 15 wt% TiH$_2$	
5TiH$_2$-10	Al + 5 wt% TiH$_2$	10 min milling

HEBM of the reactive mixtures was performed in a planetary ball mill "Activator-2S" (Novosibirsk, Russia). Two 18 g batches of Al +TiH$_2$ + 1 wt% stearic acid were loaded in 250 ml stainless steel jars partially filled with 360 g of 6 mm stainless steel balls (milling media). Before the milling, each jar was sealed, vacuumed, and filled with 99.998% pure argon (P = 400 kPa). The jar's frequency was 694 rotations per minute (rpm) at a rotational coefficient of K = 1. TiH$_2$ powder was added in the following concentrations: 1, 1.5, 5, 10, or 15 wt%. All samples were obtained by the following scheme: TiH$_2$ was pre-milled for 5 min to decrease its size, then the Al and stearic acid were added, with the mixture milled for an additional 10 min. One additional composition (5% TiH$_2$) was prepared without pre-milling of TiH$_2$ to ascertain the impact of particle size on the structural evolution of the composite. All sample abbreviations, compositions, and regimes are summarized in Table 1.

The post-milled powders were consolidated into Al-MMC disks with a diameter of 30 mm and a thickness of 6–8 mm in the vacuum using an SPS device (Labox 650, SinterLand, Japan). A load of 50 MPa was continuously applied to the sample during the process. The heating rate was 100 °C/min. Consolidation was conducted at 600 °C with a dwelling time of 20 min

The phase composition of the fabricated materials was studied through X-ray diffraction (XRD) analysis on a DRON-4–07 apparatus (Russia) using monochromatic Cu-Kα radiation (λ = 0.154187 nm). XRD patterns were scanned from 30° to 110° (2Θ) in a step-by-step scanning mode with a scan increment of 0.01°. The exposure time was 2 s. The instrumental broadening of the peaks was calibrated using Si etalon.

Phase evolution upon heating of the reactive powders was monitored in situ using the ARL X'TRA diffractometer with a Bragg-Brentano 2Θ geometry using a high-temperature add-on HTК2000 "Anton Paar". XRD patterns were recorded using Cu source (40 kV voltage and 40 mA current) and Peltier detector. A uniform 100 μm-thick layer of reactive powders was deposited onto the tungsten heater (9x10 mm^2); then the add-on was evacuated to a residual pressure of 10 Pa. The heating regime was programmed using a Eurotherm 2604 controller. The temperature was controlled by a WR5/20 thermocouple attached to the lower surface of the tungsten heater. The powder was heated at a rate of 100 °C/min with the tungsten heaters located inside the furnace chamber. Annealing of the powder was performed in a temperature range of 300–600 °C with a step of 50 °C. XRD patterns were recorded with 0.04° steps and exposure time of 6 s per step using monochromatic Cu-Kα radiation.

The microstructure of the samples was analyzed using a scanning electron microscope (SEM) Jeol JSM7600F (Jeol, Japan) equipped with an energy dispersive X-Ray spectroscopy (EDS) microanalysis system (INCA SDD 61 X-MAX, Oxford Instruments). SEM imaging and EDS analyses were performed at an acceleration voltage of 15 keV.

The thermal behavior of the ball-milled powder mixtures was investigated using differential scanning calorimetry (DSC) on a Setaram Labsys calorimeter in an Ar atmosphere. The measurements

for all experiments were collected using a crucible containing powder with an empty reference crucible for calibration. The temperature difference between the cell and sample/reference cell was measured experimentally using an S-type (platinum: platinum-rhodium) thermocouple. The measurement error was ± 1 °C. The experiments were carried out in the 20–800 °C temperature range at a constant heating rate (1 °C/s).

The microhardness of the synthesized composites was measured using Vickers hardness tests with an Emco-Test DuraScan 70 (Austria) under applied loads of 9.8 N.

Mechanical properties of the samples at room (25 °C) and elevated (500 °C) temperatures were investigated on an Instron 300LX test machine equipped with a radial furnace. For these experiments, $6 \times 4 \times 4$ mm^3 rectangular samples were prepared. To equalize the sample`s temperature with the furnace temperature, it was placed inside the preheated to 500 °C furnace and held for 10 min before the experiment. The temperature of the samples was controlled by the

K-type thermocouple attached to the surface. For each point at least 3 specimens were tested.

3. Results and discussion

3.1. Characterization of the reactive mixture after high-energy ball milling

The composite powders produced by HEBM had platelet-like and irregular-shaped morphology, typical for the mechanochemically treated Al-based powder compositions (Fig. 1a,b, Supplementary Table S1). Since aluminum is a ductile metal, multiple cold welding and fracturing events occur under the impact of the milling media, resulting in the formation of small particles (less than 10–20 µm) and larger agglomerates (50–100 µm) (Fig. 1c,d). Pre-milling of the titanium hydride decreases its particle size (see Supplementary Table S1), which along with the further treatment with Al allow the
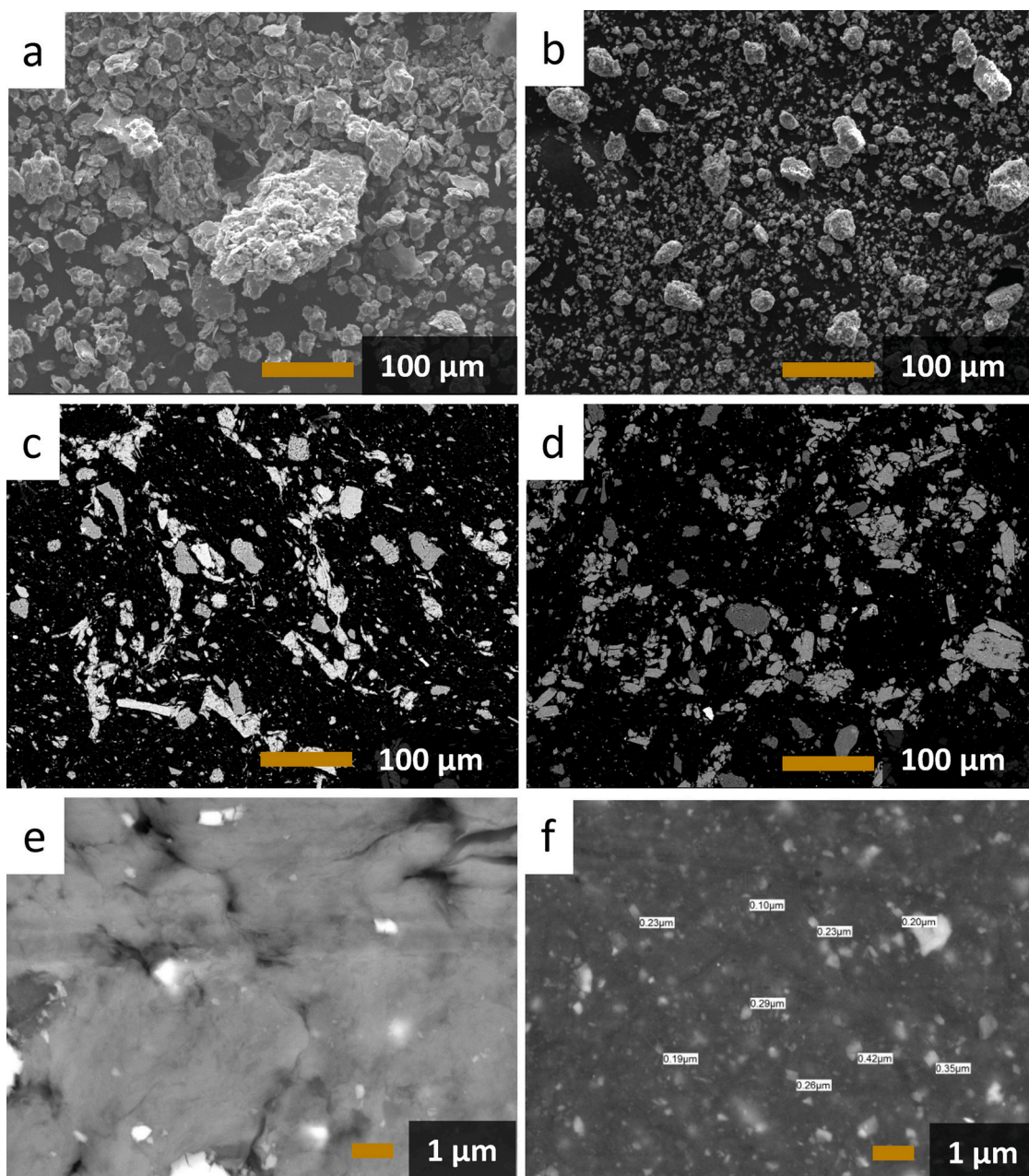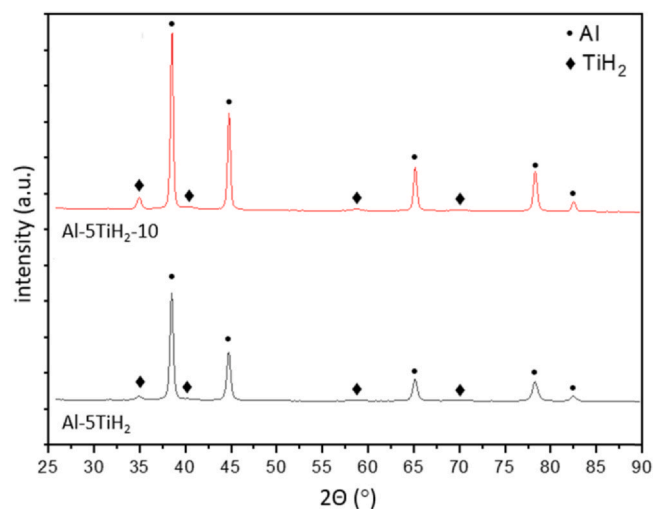

Fig. 1. SEM images and cross-sections of the composite powders produced by HEBM: (a) 5TiH$_2$–10 and (b) 5TiH$_2$.

Fig. 2. XRD patterns of Al-5%TiH$_2$ powders after different treatment regimes: 5TiH$_2$ - HEBM with 5 min of TiH$_2$ pre-milling + 10 min of the joint milling with Al; 5TiH$_2$-10 - HEBM of TiH$_2$ with Al for 10 min.

Fig. 3. XRD patterns of the Al-composites after hot pressing at 600 °C: 5TiH$_2$ and 5TiH$_2$-10.

formation of the TiH$_2$ grains less than 1 μm in size (Fig. 1e,f). The inner structure of the particles demonstrates the embedding of fine TiH$_2$ particles into the Al matrix and its uniform distribution in the Al matrix.

XRD analysis (Fig. 2) of as-milled mixtures revealed that the 5TiH$_2$-10 sample shows reflections from both Al and TiH$_2$. As the milling duration is increased, the TiH$_2$ peaks are broader and have decreased intensity, due to the decreased crystalline size and microstrain accumulation. Indeed, SEM observation showed considerable refinement of TiH$_2$ particles, which corresponds to the XRD-derived decrease of crystalline size from 277 to 99 Å. No additional phases were formed during HEBM.

Additionally, the TiH$_2$ particles upon HEBM can experience a partial decomposition. Authors in [47] demonstrate that after 2 h of HEBM the TiH$_2$ phase transformed to TiH$_{1.924}$. Additional 8 h of HEBM transformed the phase to the TiH$_{1.8}$ stoichiometry. In our work, the milling duration was orders of magnitude shorter, but the jars had twice higher rotational velocity (300 rpm vs 694 rpm), so the question of the possibility of minor hydrogen release during the HEBM remains open.

3.2. Spark plasma sintering of reactive nanocomposite powders Al-TiH$_2$

To promote the interaction between Al, Al[Ti], and Ti[Al] along with precipitation of the intermetallic reinforcing phase, the SPS was carried at 600 °C with a 20 min dwelling. At this temperature, the Al flux into Ti is higher than Ti to Al [48]; in addition, the diffusion of Al into the growing Al$_3$Ti layer is faster than Ti [49]. At the isothermal stage, Al$_3$Ti precipitates rapidly, forming the bulk composite. A small portion of the solid solutions are present in the XRD pattern, but the majority of Ti precipitates as Al$_3$Ti from the Al-matrix (Fig. 3).

For the 5TiH$_2$ sample, TiH$_2$ completely disappeared after 20 min of consolidation, meaning that the conditions are sufficient for thermal decomposition of TiH$_2$ along with the reaction of the resultant Ti with Al. XRD analysis (Fig. 3) of this sample shows only the Al matrix and Al$_3$Ti reinforcing phase. In contrast, XRD of the 5TiH$_2$-10 sample shows that the Ti[Al] solid solution is still present, indicating an incomplete reaction.

Microstructural investigations (Fig. 4) confirm the XRD results (Fig. 3). Cross-sectional analysis of non-pre-milled TiH$_2$ sample shows secondary phase particles < 10 μm distributed in the aluminum matrix (Fig. 4a). More detailed investigation (Fig. 4b) at higher magnification revealed the presence of two particle types: (i)
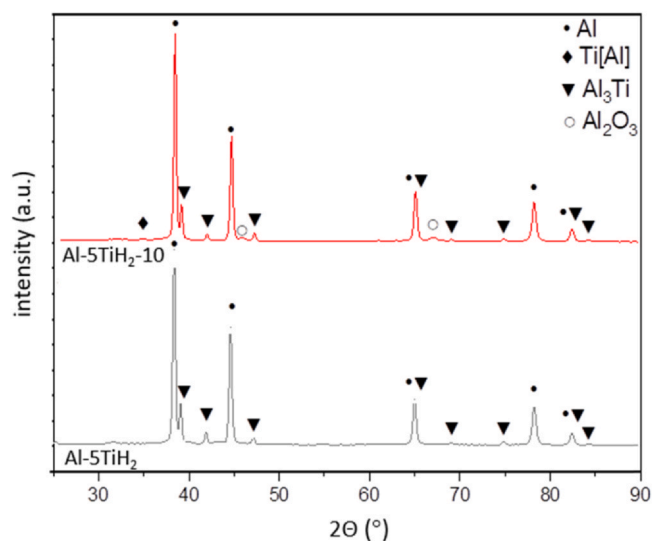
core-shell particles, with unreacted Ti covered by Al$_3$Ti, and (ii) fine Al$_3$Ti particles. This means that the sintering conditions were not sufficient for the complete conversion of these larger particles. The sample with pre-milled TiH$_2$ particles forms an Al-matrix composite with homogeneously distributed fine particles (0.02 – 0.25 μm) of the Al$_3$Ti precipitates (Fig. 4c,d). The size of Al$_3$Ti precipitates corresponds to the size of TiH$_2$ particles in the as-milled reactive composites, which opens a possibility for tailoring the microstructure of the final composite material and thus its properties. To verify the proposed phase and structural evolution mechanism of the Al-TiH$_2$ reactive nanocomposite upon heating, we conducted a series of SPS experiments followed by XRD analysis, structural investigations, and EDS distribution of Ti and Al. Samples with larger TiH$_2$ particles (such as sample 5TiH$_2$) showed a tendency towards the formation of the transitional Ti/Al$_3$Ti/Al core-shell structure (Fig. 4e,f). Conversely, when the TiH$_2$ particles were finer (such as in 5TiH$_2$-10), thinner intermetallic surface layers were formed, which were then converted into Al$_3$Ti precipitates more rapidly.

3.3. Experimental investigation of the phase formation mechanisms

To ascertain the phase transformation temperatures and kinetics, DSC experiments were conducted (Fig. 5a). The two peak positions associated with TiH$_2$ decomposition were then used for *in-situ* XRD experiments, where the intensity of the (111) TiH$_2$ peaks was monitored at a fixed temperature (Fig. 5b,c). The DSC curve has two broad endothermic peaks (350–600 °C), corresponding to the two-staged decomposition of TiH$_2$ [50–53]. The earlier onset of TiH$_2$ decomposition might result from the HEBM treatment, due to the increased defect density or smaller grain size.

The major exothermic peak on the DSC curve at ~650 °C corresponds to the precipitation of an intermetallic phase, presumably Al$_3$Ti. This was later confirmed by XRD analysis. The color-coded images depict the intensity of the TiH$_2$ (111) peak at 500 °C and 550 °C (Fig. 5d) showing an accelerated reduction in the peak intensity coupled with peak broadening during annealing at 550 °C. Al3Ti precipitation.

Heating the sample between 300 and 500 °C did not lead to any apparent phase transformation (Fig. 6a). In this range, only Al and TiH$_2$ phases were apparent (W is a material of the heater). More precise investigation of the sample before and after heat treatment showed that the TiH$_2$ peak intensity decreased, while the second peak shifted towards smaller angles, it was assumed that the
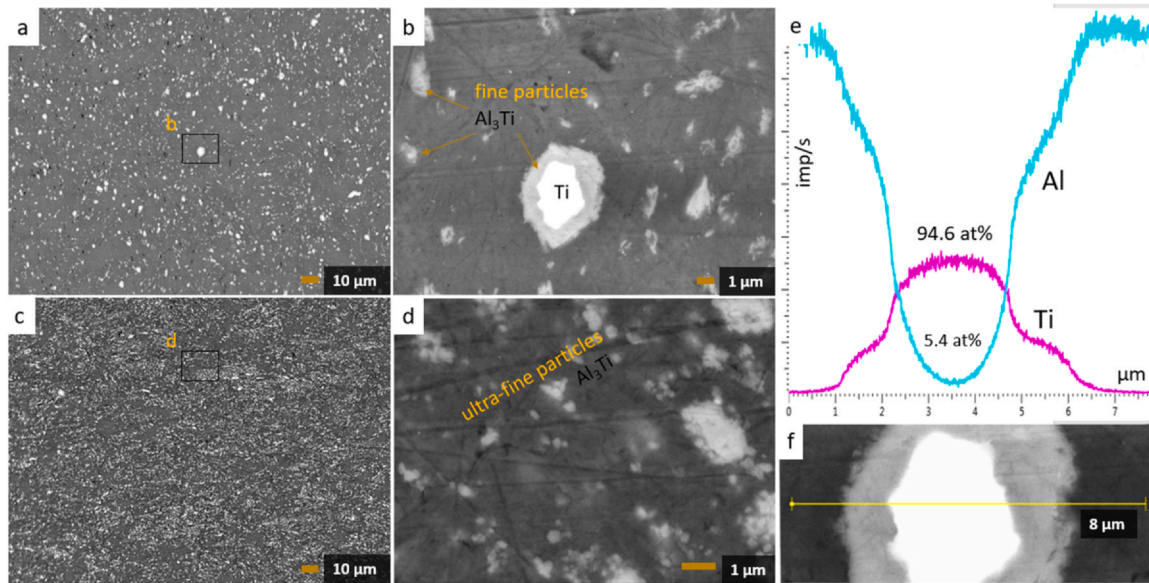
Fig. 4. SEM cross-section of bulk Al-Al$_3$Ti composite from a, b – 5TiH$_2$-10; c, d – 5TiH$_2$ and e, f – distribution of Ti (pink) and Al (teal) along the transitional Ti/Al$_3$Ti/Al core-shell structure. Samples were sintered at 600 °C.

formation of a Ti[Al] solid solution occurred. This was confirmed after annealing the powder in vacuum for 280 min at 500 °C (Fig. 6): the Al reflections became more pronounced but shifted and their lattice parameter increased, which is typical for solid solution formation. Another possible explanation for the emergence of the second peak could be the recrystallization of TiH$_2$ into a more stoichiometric phase.

The first indication of the Al$_3$Ti intermetallic was observed when heating to 600 °C. After 500 °C, the intensity of the TiH$_2$ phase peaks starts to decrease and is negligible by 550 °C. At the same temperature, peaks at ~35° and 39° emerge, which can be identified as (*100)* and (*101)* reflections of α-Ti (#44_1294) shifted to higher lattice parameters, which is indicative of a Ti[Al] solid solution. At 600 °C the intermetallic Al$_3$Ti phase also emerges (Fig. 7).

A minor amount of alumina is also formed during the isothermal annealing due to the interaction between the aluminum and oxygen impurities in the reactive nanocomposite. The reduction of the Al$_3$Ti formation temperature from 650 to 670 °C (Fig. 5a) to 600 °C during SPS may be related to the formation of plasma spark discharge between the nanocomposite particles upon sintering.

3.4. Ab initio modeling of the phase formation mechanisms

To ascertain the phase formation mechanisms in the Al-Ti-H system, the phase formation enthalpies were calculated in an open system, from which H$_2$ can leave (Fig. 8). At 0 K, two hydrides exist in the system: TiH$_2$ and AlH$_3$. Upon heating, β and γ-AlH$_3$ transition into α – phase, and then decompose. Complete γ → α AlH$_3$ transition occurs at 100 °C [54].

For the open system, we observe a series of two-phase equilibria. The increase in temperature leads to the decrease of hydrogen content and, correspondingly, a decrease in μ$_{H2}$. The stability of intermetallics increases as the Al/Ti atomic ratio increases from Ti$_3$Al to Al$_3$Ti. Because Al$_3$Ti is highly stable, coupled with the composition, it is expected that Al$_3$Ti will precipitate during sintering.

To ascertain *in-silico* the probable phase evolution mechanism during sintering of the Al-TiH$_2$ reactive nanocomposites, we explored the stability of certain phases at different hydrogen potentials (Fig. 8). The phases are stable when the energy above the convex hull

is zero or negative. The dotted line represents the meta-stability threshold of 0.1 eV/atom [55].

The phase equilibrium in Ti-Al-H$_2$ system experiences drastic changes in two periods: -μ$_{H2}$= 3.3–3.4 eV and -μ$_{H2}$= 3.9–4.1 eV. For μ$_{H2}$= 3.3–3.4 eV; Ti, Ti$_3$Al, TiAl, TiAl$_2$, and TiAl$_3$ experience a sharp step-like decrease in the energy above the convex hull. The energy for TiAl$_3$ and TiAl$_2$ reaches negative values, meaning these phases are stable. TiAl reaches the metastability threshold at 3.55 eV. Ti$_3$Al and Ti are the last two phases to stabilize (at 3.98 and 4.1 eV, correspondingly). At 4.05 eV the energy of TiH$_2$ begins to rise, and at 4.09, TiH$_2$ becomes unstable. Interestingly, the decomposition of TiH$_2$ at 550 °C resulted in the formation of an Al[Ti] solid solution rather than an intermetallic phase (Fig. 7a), which is likely the result of the residual hydrogen content in the system being still high enough to suppress intermetallic phase stabilization (Fig. 8).

Based on the ab initio modeling, DSC, and *in-situ* XRD analysis, a phase formation mechanism during reactive sintering can be proposed. DSC investigations showed two endothermic events, which are usually related to the hydrogen release and transition to elemental Ti. For heating rate above 10 °C/min, the sequence of phase transformations upon dehydrogenation of TiH$_2$ is (Eq. 1) [56]:

$$\delta\ TiH_2 \overset{\sim 450-500°C}{\rightarrow} \beta\ Ti + \delta\ TiH_2 \overset{\sim 550-600°C}{\rightarrow} \beta\ Ti. \tag{1}$$

The exact phase transformation temperature differs among reports, which may be related to the difference in sample`s weight and purity as well as in experiment procedure (atmosphere, heating rates, etc.).

During SPS, the heating rate is 100 °C/min, which means that the suggested phase transformations can be considered. Up to 400 °C, the powder compact consists of Al particles with fine TiH$_2$ embedded within. Heating to 500 °C causes partial decomposition of titanium hydride with simultaneous hydrogen release from the particle surfaces, with the formation of Al/Ti/TiH$_2$ reaction sites. The as-formed Ti can then form a solid solution or precipitate as an intermetallic. Both our results and previous reports [48,49,57] indicate that below the Al melting point, the Al$_3$Ti phase is the most stable intermetallic and will therefore appear at the interface between Ti and Al.
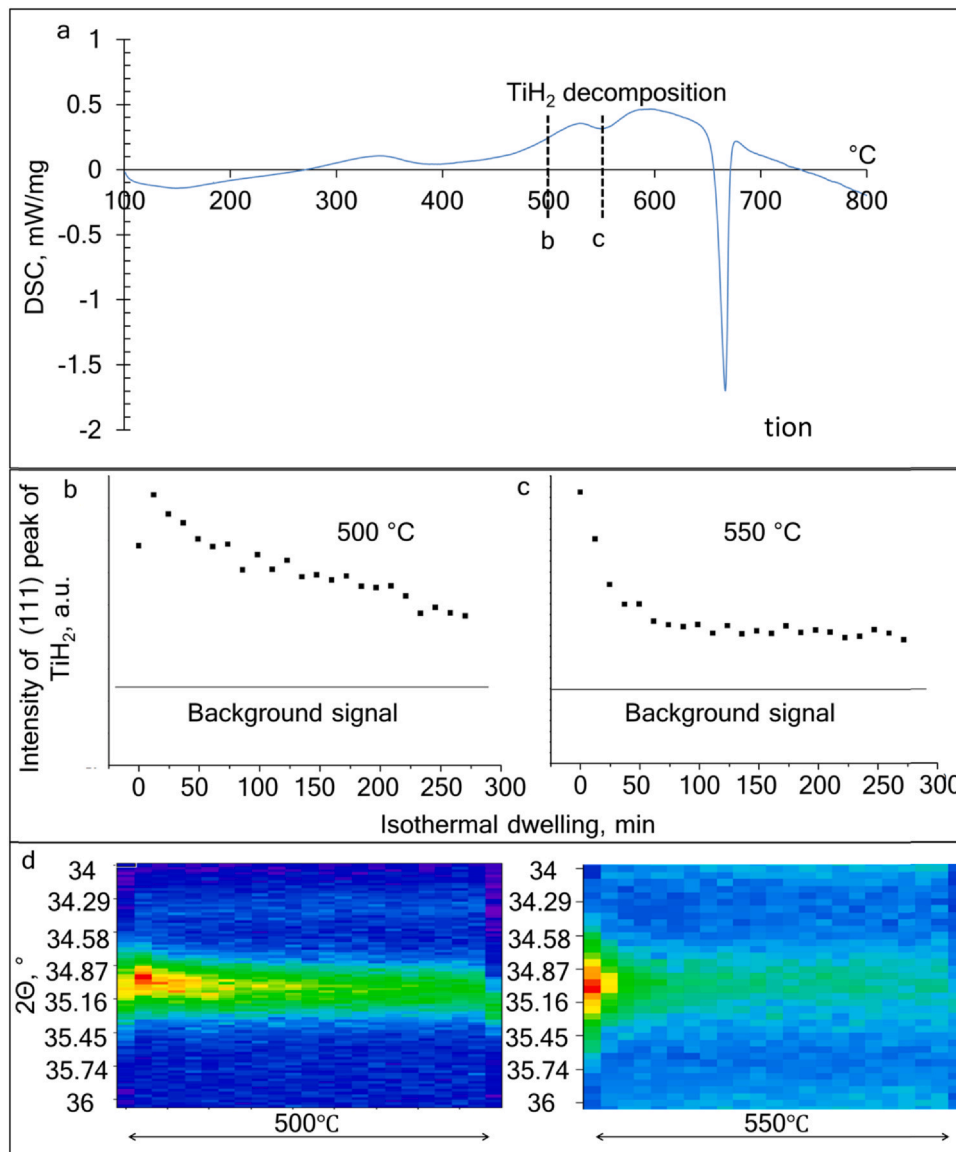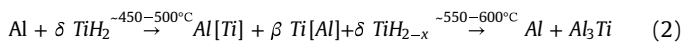
Fig. 5. DSC curve of the Al-5%TiH$_2$ reactive composite (a); extinction of 111 peak of TiH$_2$ at 500 °C (b) and 550 °C (c).

Based on the ab initio modeling and experimental observations, we propose the following phase and structure formation sequence (Eq. 2):

$$Al + \delta\ TiH_2 \xrightarrow{\sim 450-500°C} Al[Ti] + \beta\ Ti[Al] + \delta\ TiH_{2-x} \xrightarrow{\sim 550-600°C} Al + Al_3Ti \quad (2)$$

When the sintering temperature is increased to 600 °C, an intermetallic layer will grow on the Ti surface due to the diffusion of Al atoms into the intermetallic phase [49]. At this stage, the reaction will be limited by the diffusion of the Al and Ti atoms through this layer, which will lead to the formation of the core-shell transitional structures. Previous investigations [48,58] indicate that the diffusion rate of Al is ~20 times higher than Ti. As the concentration gradients continue to decrease due to the solid-phase diffusion, the transitional core-shell structures will transform into uniformly dispersed Al$_3$Ti precipitates.

3.5. Diffusion analysis and sintering guidelines for Al-TiH$_2$ reactive composites

Microstructural and phase analysis of mechanically activated reactive mixtures and sintered composite suggests that the following diffusion-related phenomena occur during the sintering: decomposition of TiH$_2$ accompanied by the release of hydrogen, diffusion of hydrogen through the as-formed Ti particles and Al matrix, diffusion of oxygen from the surface of reactive composite particles though the Al matrix, self-diffusion in Al matrix and as-formed Ti particles, interdiffusion between Al and Ti, formation of intermetallic and alumina precipitates. Additionally, pores can form in the composite as a result of the Kirkendall effect, but the application of external pressure generally counteracts the effect [59]. The formation of water vapor might also occur, leading to the formation of individual high-pressure vapor pockets; however, such pockets must be transient since the water vapor would oxidize the aluminum resulting in the formation of alumina precipitates and hydrogen outgassing.

3.5.1. Diffusion of metals and formation of Al$_3$Ti

When discussing the formation of Al$_3$Ti during the reactive sintering of Al-TiH$_2$ reactive composites, diffusion kinetics is critical in determining the interface at which Al$_3$Ti grows faster, as individual Ti and Al atoms diffuse across the intermetallic layer to react with their respective interfaces. Together with two other group IV B h.c.p.
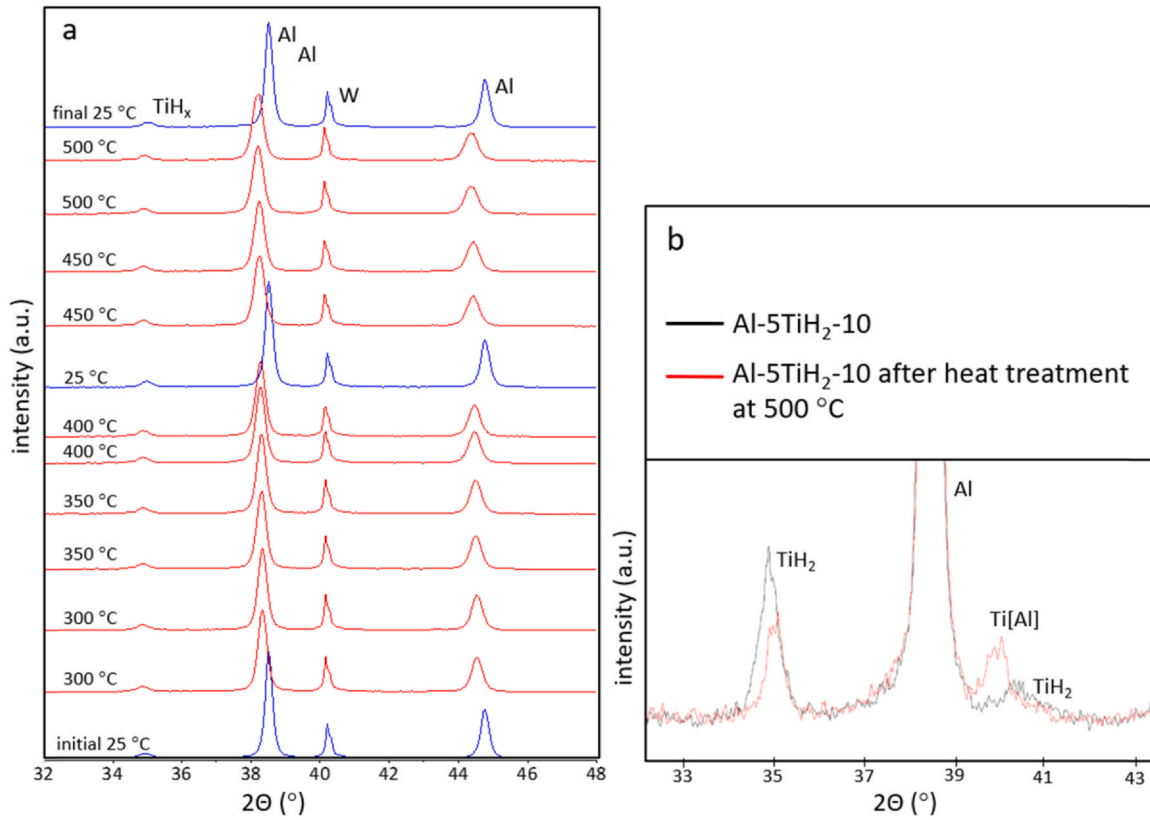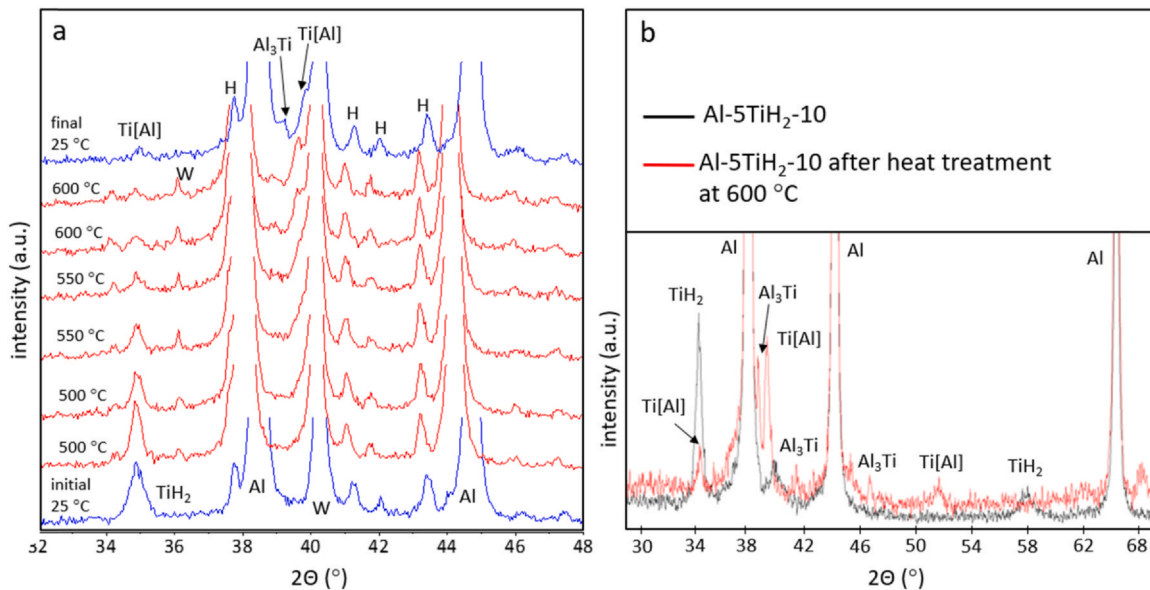
Fig. 6. The sequence of the XRD data of the 5TiH$_2$-10 sample after heat treatment in 300–500 °C temperature range (a); an overlay of the initial and final (after cooling from 500 °C) diffraction patterns (b).

metals (α - Zr and α - Hf), α - Ti is classified as an "open" metal. In such metals, the ionic-to-atomic radius ratio is unusually large in comparison with "normal" h.c.p. metals, such as Mg, Zn, and Cd [60,61]. The self-diffusion of Ti (Eq. 3) and diffusion of Al in Ti (Eq. 4) follow the Arrhenius law (T = 873–1133 K):

$$D = 1.35*10^{-3}\exp\left(-\frac{3.14}{k_B T}\right) \tag{3}$$

$$D = 6.6*10^{-3}\exp\left(-\frac{3.41}{k_B T}\right) \tag{4}$$

In this temperature range, Al diffusion into Ti particles is reported to be 3 ± 6 times slower than Ti self-diffusion. In both cases, the diffusion anisotropy ratio D$_\perp$/D$_\parallel$ is about two, which corresponds well with the c/a correlation usual for h.c.p. metals [61]. Hence, in the initial stages of the sintering (before the formation of continuous

Fig. 7. Sequence of the XRD data of the 5TiH$_2$-10 sample a) after heat treatment in 500–600 °C temperature range; b) initial and final (after cooling from 600 °C) diffraction patterns.
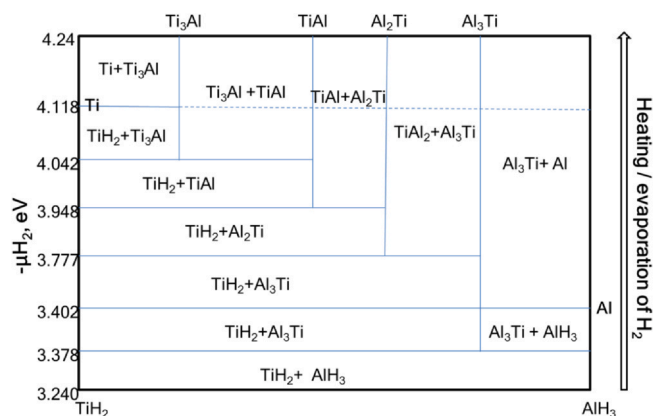
Fig. 8. Phase diagram for the Ti-Al-H$_2$ system (open to H$_2$).

Al$_3$Ti layers), the net flux of atoms should be directed from Ti particles into the Al matrix.

At both the Ti/Al$_3$Ti and Al/Al$_3$Ti interfaces, it is expected that the formation of Ti[Al] and Al[Ti] solid solutions occurs before the nucleation of Al$_3$Ti. According to the Ti-Al binary phase diagram [62], the Ti[Al] solid solution exists over a broad composition range, whereas the Al[Ti] solid solution region appears to be narrow, indicating that Al is more soluble in Ti than Ti is in Al. With this phenomenon in mind, Xu et al. [63] claimed that Al[Ti] solid solution reaches saturation earlier than Ti[Al], due to the lower solubility of Al in Ti resulting in faster nucleation of Al$_3$Ti nuclei along the Al/Al$_3$Ti interface. Additionally, it was expected that the distribution of Al$_3$Ti nuclei near the Al/Al$_3$Ti interface would be fine and uniform, whereas it would be relatively coarse on the other side [63]. On the interface between Al and Ti, the formation of a new lattice is the rate-determining step and results in a nearly-linear layer growth (Eq. 5) [59,64]:

$$d = \left(2.6^* e^{-\frac{42.9}{RT}^*}t\right)^{0.909} \tag{5}$$

where d is the diameter of particles (m), R is the gas constant.

When a certain intermetallic layer thickness is reached, diffusion of elements through the Al$_3$Ti becomes the rate-controlling step, resulting in a parabolic growth rate [59]. Vacancies act as a key mediator in the diffusion in Al$_3$Ti [65]. Zhu et.al. [66] calculated migration barriers for the Al and Ti in the Al$_3$Ti lattice. They demonstrated that the lowest possible migration energy barrier of Al vacancy is 0.54 eV, corresponding to the jump of the vacancy to the first nearest neighbor site. Ti vacancy cannot jump effectively via inner sublattice hop due to the high migration energy of 5.89 eV. The first nearest neighbor hop has lower migration energy of 1.41 eV but would cause the disorder of the Al$_3$Ti crystal structure. Considering the prohibitively high migration energy of inner sublattice hop for Ti vacancy, Zhu et.al. [66] proposed a diffusion mechanism that involves the net migration of a two-defect complex. The migration path consisted of one second nearest neighbor hop of Ti vacancy, two first nearest neighbor hops of Al vacancy, and one second nearest neighbor hops of Al vacancy. The largest migration energy barrier of 1.70 eV for this two-defect complex hop sequence occurs in the second nearest neighbor hops of Al vacancy and is significantly decreased compared with the migration energy of direct inner sublattice hop for Ti vacancy (5.89 eV). These findings were corroborated by Thiyaneshwaran et al. [48] who reported that Al was diffusing almost 20 times faster than Ti through the Al$_3$Ti layer.

Microstructural investigation of sample 5TiH$_2$-10 revealed the presence of transitional Ti/Al$_3$Ti/Al core-shell structures in places where relatively large TiH$_2$ particles were in the reactive composites (Fig. 4b). The microstructural analysis of these core-shell structures

(Fig. 4f) shows that the Al$_3$Ti/Al interface contains multiple nano-sized Al$_3$Ti precipitates, whereas the Ti/Al$_3$Ti interface is smooth, with no precipitates present in the area. The linear EDS scan of the core-shell structure (Fig. 4e) suggests that the Ti-based particle is Ti-5 at% Al solid solution, whereas the surrounding Al matrix has little to no dissolved Ti atoms. While the numerical values of the elemental composition of Ti-based particles should be treated with a grain of salt due to the possibility of the background emission from the Al matrix, this result agrees well with the previously published data on the solubility of Al in Ti [62,63]. One should note, however, that Thiyaneshwaran et al. [48] reported a different precipitation mechanism in multilayered Ti/Al diffusion pairs, with Al$_3$Ti particles forming on the Ti/Al$_3$Ti interface and Al/Al$_3$Ti interface being smooth.

The difference can be attributed to two factors: (1) localization of Ti as inclusion in Al matrix instead of parallel Ti and Al layers, used by Thiyaneshwaran et al. [48]; (2) application of anisotropic external pressure during the hot pressing as compared to vacuum annealing employed in the diffusion couple studies. The TiH$_2$ particles (ρ = 3.75 g/cm^3) first transform into Ti (ρ = 4.5 g/cm^3), then into Ti[Al] solid solution ($\rho \approx$ 4.41 g/cm^3), and finally into TiAl$_3$ (ρ = 3.3 g/cm^3). The outgassing of hydrogen accounts for a 2.7–4.1 wt% decrease in the weight of the initial TiH$_2$ particles. Overall, the conversion of TiH$_2$ into Al$_3$Ti leads to a 12% increase in the volume of the reinforcing phase. If the growth of the Al$_3$Ti layer was achieved by diffusion of Al though Al$_3$Ti layer into saturated Ti[Al] solid solution, the precipitation of emerging Al$_3$Ti grains on the Ti/Al$_3$Ti interface would create massive tensile stress due to the drastic difference in the density of Ti[Al] and Al$_3$Ti. This stress can either lead to continued fragmentation of the Al$_3$Ti layer or arrest the precipitation of Al$_3$Ti on the Ti/Al$_3$Ti interface, making the diffusion of Ti (or Ti vacancies) through the Al$_3$Ti layer an overall rate-limiting step. The interdiffusion coefficient of Ti in Al$_3$Ti was previously established as 1.202·10^{-15} m^2/s at 575 °C [48] and was taken as a reasonable approximation for the sintering conditions employed in our work.

The two-dimensional Einstein's relation can be applied to calculate the relations between the diffusion length and sintering duration (Eq. 6):

$$D = s^2/4t \tag{6}$$

where D is the diffusion coefficient (1.202·10^{-15} m^2/s), s is the diffusion length (m), and t is the time (s). We assume that the diffusion coefficient is a single-valued function of the concentration of a given element. This is always the case, if an undisturbed single diffusion mechanism is operating, no matter whether this is volume diffusion or e.g. grain-boundary diffusion. In most metals, this requirement is fulfilled at temperatures higher than half the absolute melting point. The required diffusion length is taken as half of the particle's effective diameter. To provide tentative guidelines for the optimization of Al-TiH$_2$ sintering conditions we calculated the relationship between the diameter of initial TiH$_2$ particles and the dwelling time required for their complete conversion into Al$_3$Ti (Fig. 9).

The results correspond well with our microstructural observations - at the selected sintering duration of 20 min, TiH$_2$ particles larger than ~4 µm formed transitional Ti/Al$_3$Ti/Al core-shell structures, whereas finer particles were completely converted into Al$_3$Ti (Fig. 4b,d). Naturally, the differences in the kinetics of diffusion and Al$_3$Ti precipitation kinetics led to the drastic alteration in the microstructure of sintered composites. For example, the average size of Al$_3$Ti precipitates in the 5TiH$_2$-10 sample is 1040 nm, whereas in the 5TiH$_2$ sample (with pre-milled TiH$_2$) it is 208 nm. This corresponds to a ~125 increase in the interface area between Al matrix and Al$_3$Ti precipitates. The increase of TiH$_2$ content up to 15%, however, results in the increase in the size of the Al$_3$Ti precipitates to 1215 nm, probably due to the recrystallization of Ti and Al$_3$Ti during sintering. As will be demonstrated in **Section 3.6** , the difference in the size of
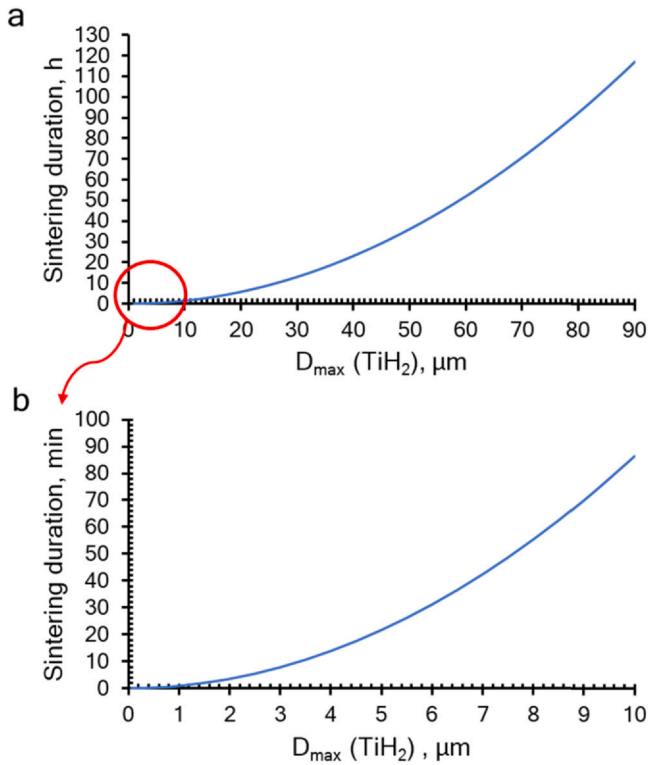
Fig. 9. Calculated relation between the maximum diameter of TiH$_2$ particles in the Al-TiH$_2$ mixture and time required for the complete conversion of TiH$_2$ to Al$_3$Ti at 600 °C.

Al$_3$Ti is closely related to the mechanical performance of the sintered composites.

3.5.2. Diffusion of hydrogen and oxygen during sintering of Al-TiH$_2$ composites

The usage of TiH$_2$ in the Al-TiH$_2$ reactive composites raises the question of hydrogen embrittlement of the resulting Al-Al$_3$Ti material. Hydrogen can interact with various microstructural defects in aluminum (including significant hydrogen-vacancy interactions) and can become trapped in the Al matrix. The mechanisms of embrittlement are not fully understood yet but may include hydrogen-induced local plasticity and decohesion, as well hydriding and stimulation of vacancy formation. The combination of these factors can degrade the mechanical behavior of the materials under both static and cyclic loading [67].

It should be noted that the diffusion of hydrogen in aluminum is significantly affected by the presence of Al$_2$O$_3$ both in the form of oxide films on the surface of the Al particle and Al$_2$O$_3$ grains. Surface oxide films can form on aluminum particles even in a vacuum and have a significant effect on hydrogen permeability. The relationship between hydrogen permeability and annealing duration shows that reconstruction of the metal-oxide interface results in the creation of crystalline Al$_2$O$_3$ particles [68] and alters the process's limiting step. With an increasing fraction of Al$_2$O$_3$ particles at the metal-oxide interface, the effective cross-section for hydrogen diffusion through the metal decreases.

This explains why the hydrogen flow rate through aluminum decreases during high-temperature annealing. When the majority of the 'aluminum–aluminum oxide' interface is covered with crystalline Al$_2$O$_3$ particles, the mechanism of hydrogen transfer through aluminum changes. Following this point, the rate of hydrogen adsorption on the metal-oxide interface begins to dictate the pace of hydrogen penetration into the metal. Correspondingly, the reaction has a zero-order at high pressures, as well as the increased activation energy of hydrogen permeability in aluminum following a long

period of high-temperature annealing. These modifications may not affect the mode of the aluminum permeability to hydrogen dependency on hydrogen pressure if they occur in the oxide film but not at the metal-oxide interface. Simultaneously, gas porosity kinetics is dependent on the pace of hydrogen redistribution inside the metal structure after heat treatment. Based on the formation of ~4 wt% Al$_2$O$_3$ after the sintering of Al-TiH$_2$ samples, we estimate the content of O in the mechanically activated mixture at 2 at%.

Hydrogen and oxygen both dissolve in α-Ti, forming interstitial solid solutions. The effect of these two elements on the metallic matrix structure, on the other hand, is quite different. Oxygen's high solubility (34 at%) stabilizes the compact hexagonal α-phase, with O atoms taking up octahedral positions in the crystal lattice. Hydrogen, which is nearly insoluble in the α-phase (0.14 at%), where it occupies tetrahedral sites, dissolves much more easily in the cubic β-phase, thereby increasing its heat stability. When oxygen diffusion occurs in Ti-H, the primary effect is the disappearance of hydrides when the oxygen concentration exceeds 2 at% (for H-rich titanium hydrides) and 5 at% (for H-depleted titanium hydrides). Hydrogen's diffusion conditions are highly dependent on the oxygen content in the system. A concentration of 1–2 at% appears to be critical; at higher oxygen concentrations, the amount of dissolved hydrogen significantly decreases, which is beneficial for the prevention of hydrogen embrittlement [69].

In the case of the sintering of Al-TiH$_2$-absorbed O, the H outgassing and formation of Al$_2$O$_3$ is affected by the length of the diffusion pathway between the source of the gas (the decomposing TiH$_2$ particles in case of H and surface of reactive composite particles in case of O).

According to [70], the solubility of hydrogen in aluminum L [cm^3/ 100 g] is (Eq. 7):

$$\lg L = -\frac{2080}{T} + 0.788 + \frac{1}{2}\lg P \tag{7}$$

where P is pressure [atm]. For the used pressure of 50 MPa and temperature of 600 °C the calculated hydrogen solubility is 0.035 cm^3/100 g of Al matrix and drops dramatically with the decrease of temperature.

Regarding the temperature dependence of the hydrogen diffusion coefficient in aluminum, there is a relatively wide scattering in the data reported in various sources (Fig. 10). The discrepancies in the hydrogen diffusion coefficients and the activation energy values might be caused by differences in the used materials, as well as by not accounting for surface-absorbed and captured-by-traps
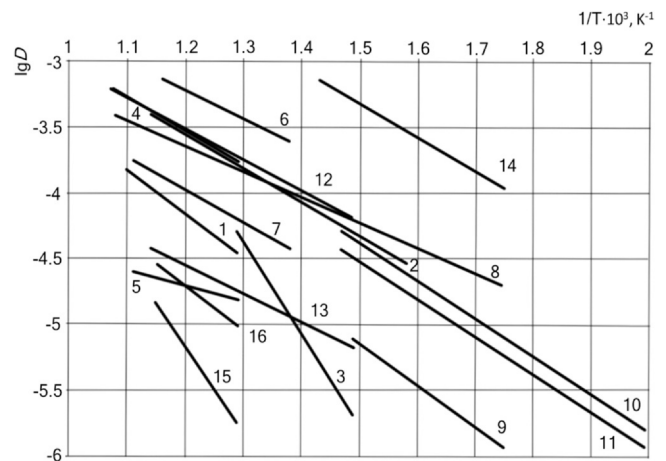
Fig. 10. A compilation of hydrogen diffusion in aluminum.
Data from various sources: 1 – [70]; 2 – [71]; 3 – [72]; 4 – [73]; 5 – [74]; 6 – [75]; 7 – [76]; 8 – [77]; 9 – [78]; 10 – [79]; 11 – [80]; 12 – [81]; 13 – [82]; 14 – [83]; 15 – [84]; 16 – [85].

hydrogen. The evolution of gas porosity is highly dependent on the hydrogen content of the metal. Metals can degas during heat treatment in air, an inert atmosphere, or under vacuum.

The sintering duration required for complete degassing of Al-TiH$_2$ reactive composites depends on the weight fraction of the TiH$_2$ in the mixture, temperature, the size of reactive agglomerates, and the porosity (and pore structure) of the sintering powder body. TiH$_2$ particles contain 2.7–4.1 wt% H$_2$ (depending on their stoichiometry). In situ XRD investigations and DSC analysis (Figs. 5–7) suggest that to achieve a complete decomposition of TiH$_2$ at a reasonable sintering time, temperatures of 550–600 °C are required. The diffusion path required for hydrogen to exit the material depends on the pore structure of the powder body.

Let's consider two extreme cases: (1) The decomposition of TiH$_2$ and hydrogen outgassing completes while the particles of the reactive composite are still connected with open porous canals; and (2) The TiH$_2$ decomposition and outgassing occur after the pores in the powder body have been closed and isolated by recrystallizing Al matrix. In the former case, the diffusion length is equal to the effective radius of the reactive composite particle (r_{rcp}), whereas in the latter case the hydrogen has to diffuse through Al the whole distance between the particular TiH$_2$ inclusion and the surface of the sample. Taking into account the relatively uniform distribution of TiH$_2$ inclusions within the powdered body, the diffusion length, in this case, is roughly equivalent to ¼ of the sample's height and is at least 2 orders of magnitude higher than r_{rcp}.

To ascertain the required duration of dwelling without the application of pressure, we used the Einstein's relation (Eq. 4) and a middle-of-the-road estimation of hydrogen's diffusion coefficient, obtained by Ulanovsky [70] at 600 °C (Eq. 8):

$$D = 0.525 \cdot \exp\left(-\frac{62002}{RT}\right) \tag{8}$$

where R = 8.314 (J/mol·K).

The calculations show that the diffusion of individual hydrogen atoms from TiH$_2$ particles to the surface of specimens at 600 °C takes from $6 \cdot 10^{-6}$ to 24.5 s depending on the position of TiH$_2$ particles and the sintering stage. Since the rate of hydrogen outgassing depends not only on the diffusion mobility but also on the release rate, we used the estimations of the 50% transformation ($t_{0.5}$) of the titanium hydride derived from in situ XRD study performed in this work and in [86]. At 600 °C, the $t_{0.5}$ is ~20 min both in this work (Fig. 5c) and in the reference [86]. At 600 °C, the $t_{0.5}$ decreases to ~8 min. Using these values, we calculated the duration of sintering (Fig. 11) which is required for the reactive composite to achieve a residual hydrogen content below the solubility of hydrogen in Al at the given sintering temperature and pressure (Eq. 5) depending on the TiH$_2$ content in
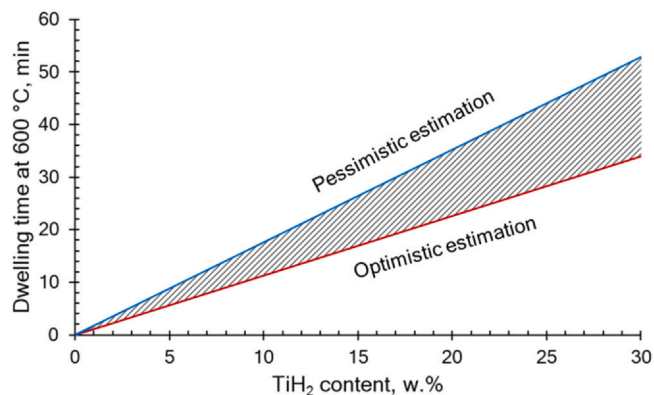

Fig. 11. Optimistic and pessimistic estimations of the dwelling time (min) required for complete evacuation of hydrogen from the sintering Al-TiH$_2$ reactive composites.

the reactive composite (0–30 wt%). The dwelling time of 20 min chosen in this work lies either above the pessimistic estimation or between the pessimistic and optimistic estimations (Fig. 11), depending on the composition. A sample height of 10 mm was assumed for the calculations, but the sintering time can be scaled linearly to fit the required geometry.

3.6. Mechanical properties of spark plasma sintered Al-Al$_3$Ti composite

To understand how the initial TiH$_2$ content affects the mechanical performance of the spark plasma sintered composites, samples with 1–15% TiH$_2$ content were produced. The SPS samples were then used for the preparation of mechanical test specimens at room and elevated temperatures. The ultimate tensile strength (UTS) and yield stress (YS) for Al-MMC with different TiH$_2$ addition are shown in Fig. 12. Compared to pure Al and Al after HEBM [87], the mechanical properties were improved by *in-situ* Al$_3$Ti reinforcement. At room temperature, the maximum UTS and YS reached 437 ± 26 and 367 ± 32 MPa respectively for 1.5TiH$_2$ and 410 ± 29 and 337 ± 34 MPa for 5TiH$_2$ samples, which is 4 times higher than pure Al (92 MPa [87]).

As the reinforcement additive content increases from 1% to 15%, a more effective transfer of stress from the matrix to reinforcing particles is induced. Enhancement in the strength can partially be attributed to Orowan strengthening, which is based on the deceleration of the dislocations on second phase particles [88]. However, the grain-boundary strengthening (Hall-Petch strengthening) may play an even more important role in the enhancement of the mechanical properties due to reduction of the Al grain size after HEBM, since its size may be several times less compared to the effective distance between reinforcing particles [89]. To confirm the latter hypothesis, we conducted a TEM investigation of the two samples: pure Al (ASD-6 grade) and 5TiH$_2$, which we sintered in the same conditions (Fig. 13). Grains in the sintered pure Al powder have an ovoid shape and a size of 2–3 μm (Fig. 13a). For the 5TiH$_2$ composite the microstructure changes drastically, it is almost impossible to determine the grain size at the same magnification (Fig. 13b). Investigation at higher magnification revealed the formation of the nanocrystalline Al grains (Fig. 13c) along with the Al$_3$Ti inclusions. Further detailed analysis showed that a clean interface without any visible porosity or defects was formed between the aluminum matrix and reinforcement particles.

The decrease of the mechanical properties with an increase in the amount of additive over an optimal value can be associated with the clustering of the additives leading to its inhomogeneous distribution and deterioration of the composite's mechanical performance at room temperature [90]. For the 5TiH$_2$-10 sample, relatively low strength values can also be associated with the incomplete conversion of Ti into Al$_3$Ti. In stark contrast, the highest high-temperature mechanical properties (Supplementary Table S2) were achieved for the composition with 15TiH$_2$, in which a relatively high concentration of Al$_3$Ti was accompanied by the presence of individual transitional core-shell Ti-Al$_3$Ti-Al structures (Supplementary Fig. S2). This effect can be attributed to two factors: (1) significantly increased content of Al$_3$Ti phase, which provides considerably higher creep resistance but also contributes to composite's embrittlement at room temperature due to dislocation pinning; (2) in situ transformation of transitional core-shell Ti-Al$_3$Ti-Al structures into new Al$_3$Ti precipitates, which leads to *in-situ* toughening and grain refinement at elevated temperatures. A similar effect was previously reported for ceramics with transitional core-shell microstructural elements [91]. The underlying diffusion mechanisms are discussed in **Section 3.5** . Please note that the presence of transitional core-shell Ti-Al$_3$Ti-Al structures in the sample with 15% TiH$_2$ correlates well with the proposed sintering guidelines (Fig. 11) since the sintering time is below the pessimistic estimation for the composition.
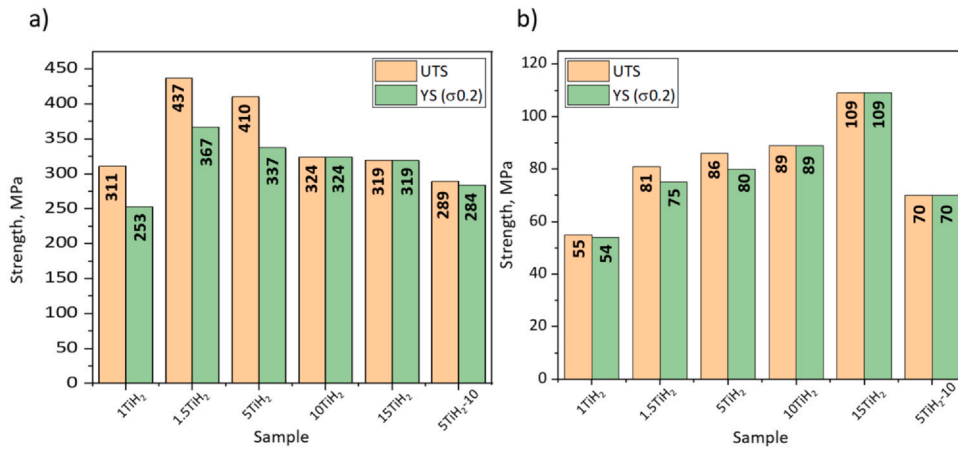
Fig. 12. Ultimate tensile strength (UTS) and yield stress (YS) for Al-MMC with different TiH_2 addition, with tensile testing conducted at (a) room temperature and (b) 500 °C.

A good trade-off was achieved for $5TiH_2$, which had high values of UTS and YS, along with decent plasticity (6% elongation of the sample before fracture).

Fig. 14 shows the $5TiH_2$ sample after tensile testing at different temperatures. The fracture trajectory at the macro-level (Fig. 14a,b) in both cases is close to linear, with no pronounced signs of macro-
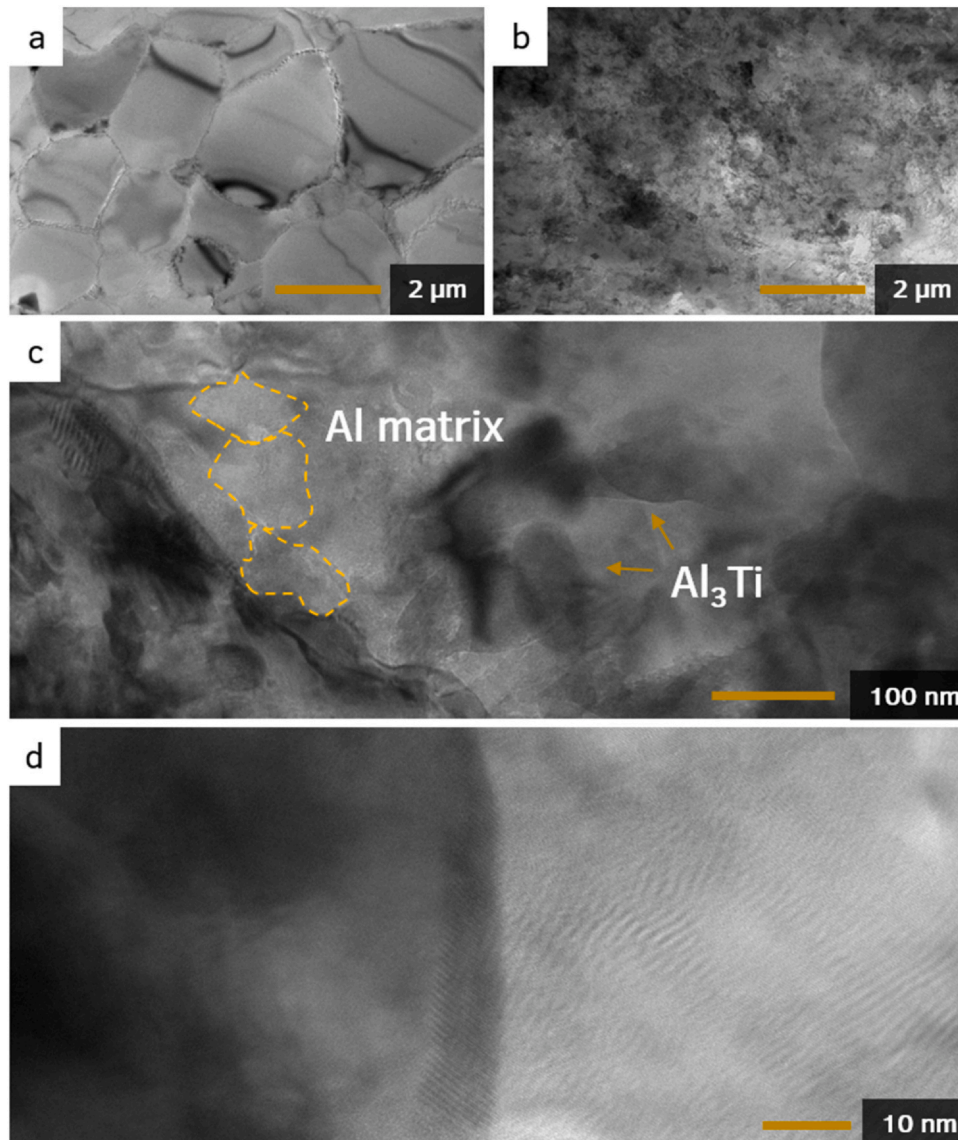

Fig. 13. TEM micrographs of the pure Al (a) and $5TiH_2$ (b,c,d) sintered samples.
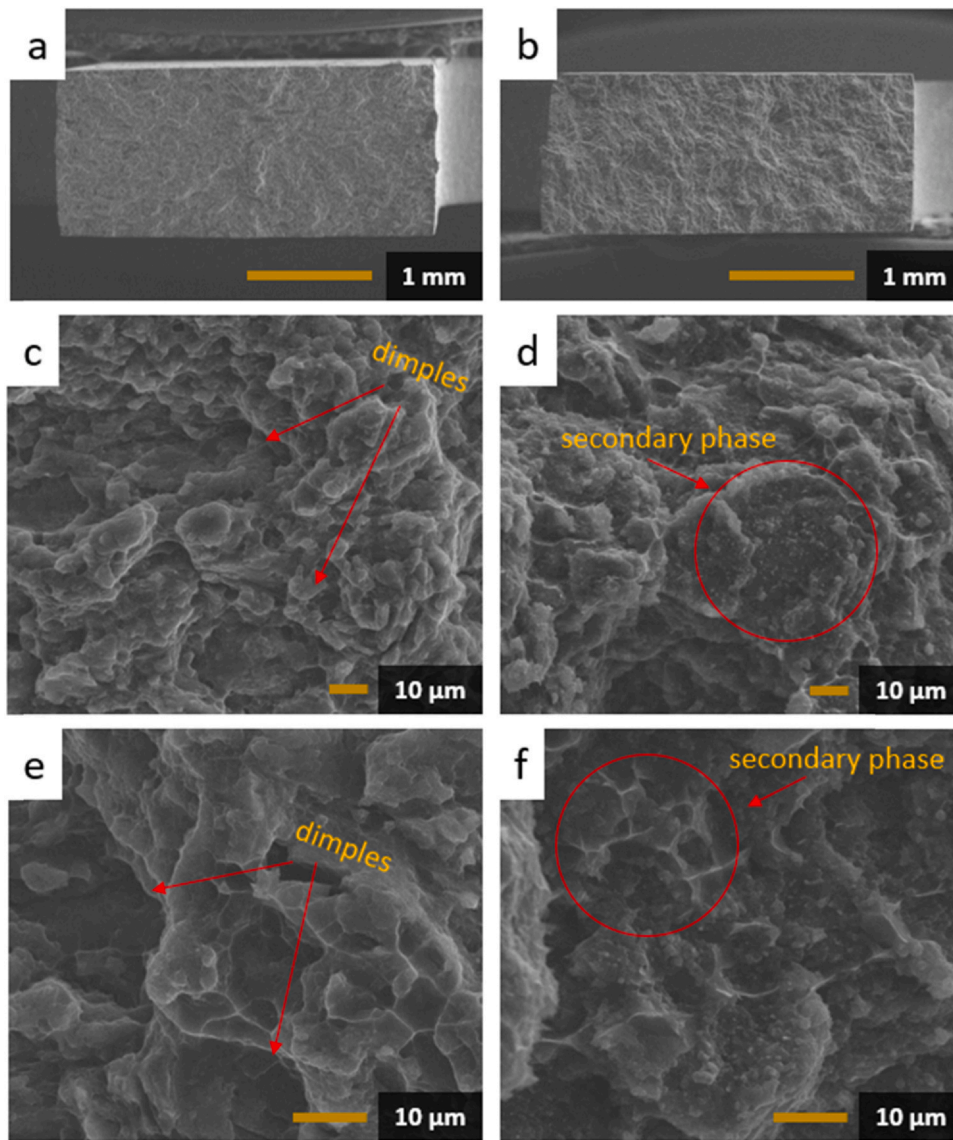
Fig. 14. SEM images of the fracture surface of the 5TiH$_2$ sample after tensile tests at room temperature (a,c,e) and 500 ℃ (b, d, f).

scale plastic deformation. Correspondingly, stress-strain curves of these samples have an almost linear character, indicating fracture without noticeable elongation (Supplementary Fig. S3). During the brittle fracture, the cracks propagate through the sample at high velocity (up to 0.4–0.5 of the speed of sound). Higher magnification revealed the presence of the dimples (red arrows at Fig. 14c,e) and fractured surfaces, implying the prevalence of ductile deformation at the microlevel. Such microstructure results from the formation of the microvoids in local volumes of the sample during the stress-induced loss of stiffness. For tests at elevated temperatures (Fig. 14d,f), areas with the secondary phase inclusions (red ring on the Fig. 14d) and ridges (red ring on the Fig. 14f) are also observed with the dimple formation. This indicates that destruction occurred by the formation of the transgranular cracks. In general, it can be concluded that the resulting fracture pattern shows a mixed brittle-ductile deformation behavior. It should be noted that measured UTS and hardness for our MMCs are significantly higher than previously reported values (Table 2). For example, composite containing 2.5 wt% Al$_3$Ti (1.5TiH$_2$) demonstrates a 50% higher UTS value compared to those with increased intermetallic phase content Al-(15–50 wt%)Ti.

Table 2
UTS and hardness at room temperature of Al-based MMCs.

Composition	Al$_3$Ti content, wt%	UTS, MPa	Hardness HV, GPa	Reference
Pure Al	0	92	28	[87]
Pure Al after HEBM	0	167	44	
Al - 4.5 wt%BN	–	386	124	
Al - 8 wt% Al$_3$Ti	8	449	–	[26]
Al - 5 vol% Al$_3$Ti	6	311	–	[92]
Al - 20 wt% Ti	~ 50	–	136	[29]
Al - 5 wt% Ti	~ 15	287	–	[28]
Al - 20 wt% Ti	~ 50	300	164	[27]
Al - 5 wt% Ti	~ 15	313	98	[21]
Al - 1.5 wt% TiH$_2$	2.5	437	155	this work
Al - 5 wt% TiH$_2$	8.5	410	190	this work

4. Conclusions

Based on ab initio calculations, DSC analysis, *in-situ* XRD studies, analysis of diffusion kinetics, and structural observations, the following phase, and structure formation mechanism was proposed:

$$Al + \delta\ TiH_2 \xrightarrow{\sim 450-500°C} Al[Ti] + \beta\ Ti[Al] + \delta\ TiH_{2-x} \xrightarrow{\sim 550-600°C} Al + Al_3Ti.$$

Using this fundamental mechanistic understanding, tentative sintering guidelines were proposed and samples were produced by spark plasma sintering of high-energy ball-milled Al-TiH$_2$, leading to an Al matrix reinforced by fine (0.05–0.25 μm) Al$_3$Ti precipitates. Samples with coarser TiH$_2$ or higher TiH$_2$ content featured a minor amount of transitional core-shell structures resulting from the incomplete conversion of the as-formed Ti particles into Al$_3$Ti. This allows for tailoring of the final microstructure of the Al-MMCs, producing Al$_3$Ti reinforcement based on the size of the TiH$_2$. The combination of HEBM and SPS allowed *in-situ* production of the Al/Al$_3$Ti composites with ultimate tensile strength up to 437 MPa at room temperature and up to 109 MPa at 500 °C, as well as a decent elongation before failure (~6%). Obtained data shows that the *in-situ* fabrication approach using HEBM and subsequent SPS allows the production of the Al-MMCs with enhanced mechanical properties compared to those for bulk Al-MMCs with Al$_3$Ti added separately. This combination of properties results from a mixed ductile-fragile deformation behavior of the investigated composites.

CRediT authorship contribution statement

S. Vorotilo: Conceptualization, Methodology, Visualization, Writing – original draft, Writing – review & editing. **A.A. Nepapushev:** Supervision, Conceptualization, Methodology, Visualization, Writing – original draft, Writing – review & editing. **D.O. Moskovskikh:** Supervision, Resources, Visualization, Writing – review & editing. **V.S. Buinevich:** Investigation, Visualization. **G.V. Trusov:** Investigation. **D. Yu. Kovalev:** Investigation. **A.O. Semenyuk:** Investigation. **N.D. Stepanov:** Conceptualization, Writing – review & editing. **K. Vorotilo:** Investigation, Visualization. **A.Y. Nalivaiko:** Investigation, Visualization. **A.A. Gromov:** Funding acquisition, Writing – review & editing.

Declaration of Competing Interest

The authors declare that they have no known competing financial interests or personal relationships that could have appeared to influence the work reported in this paper.

Acknowledgments

Declaration of competing interest

The authors declare that they have no known competing financial interests or personal relationships that could have appeared to influence the work reported in this paper.

Appendix A. Supporting information

Supplementary data associated with this article can be found in the online version at doi:10.1016/j.jallcom.2021.162676.

References

[1] J. Torralba, C. da Costa, F. Velasco, P/M aluminum matrix composites: an overview, J. Mater. Process. Technol. 133 (2003) 203–206, https://doi.org/10.1016/S0924-0136(02)00234-0

[2] M.K. Surappa, Aluminium matrix composites: challenges and opportunities, Sadhana 28 (2003) 319–334, https://doi.org/10.1007/BF02717141

[3] A. Schmidt, S. Siebeck, U. Götze, G. Wagner, D. Nestler, Particle-reinforced aluminium matrix composites (AMCs)—selected results of an integrated technology, user, and market analysis and forecast, Metals 8 (2018) 143, https://doi.org/10.3390/met8020143

[4] R. Casati, A. Fabrizi, G. Timelli, A. Tuissi, M. Vedani, Microstructural and mechanical properties of Al-based composites reinforced with *in-situ* and ex-situ Al$_2$O$_3$ nanoparticles, Adv. Eng. Mater. 18 (2016) 550–558, https://doi.org/10.1002/adem.201500297

[5] L. Xi, S. Guo, D. Gu, M. Guo, K. Lin, Microstructure development, tribological property and underlying mechanism of laser additive manufactured submicro-TiB$_2$ reinforced Al-based composites, J. Alloy. Compd. 819 (2020) 152980, https://doi.org/10.1016/j.jallcom.2019.152980

[6] A.P. Amosov, A.R. Luts, A.D. Rybakov, E.I. Latukhin, Using different powdered carbon forms for reinforcing aluminum composite materials with carbon and titanium carbide: a review, Russ. J. Non-Ferr. Met. 61 (2020) 500–516, https://doi.org/10.3103/S1067821220050028

[7] M. Hadian, H. Shahrajabian, M. Rafiei, Mechanical properties and microstructure of Al/(TiC+TiB$_2$) composite fabricated by spark plasma sintering, Ceram. Int. 45 (2019) 12088–12092, https://doi.org/10.1016/j.ceramint.2019.03.106

[8] B. Guo, B. Chen, X. Zhang, X. Cen, X. Wang, M. Song, et al., Exploring the size effects of Al$_4$C$_3$ on the mechanical properties and thermal behaviors of Al-based composites reinforced by SiC and carbon nanotubes, Carbon 135 (2018) 224–235, https://doi.org/10.1016/j.carbon.2018.04.048

[9] A.E. Steinman, S. Corthay, K.L. Firestein, D.G. Kvashnin, A.M. Kovalskii, A.T. Matveev, et al., Al-based composites reinforced with AlB$_2$, AlN and BN phases: experimental and theoretical studies, Mater. Des. 141 (2018) 88–98, https://doi.org/10.1016/j.matdes.2017.12.022

[10] A.V. Alekseev, M.A. Yesikov, V.V. Strekalov, V.I. Mali, A.A. Khasin, M.R. Predtechensky, Effect of single wall carbon nanotubes on strength properties of aluminum composite produced by spark plasma sintering and extrusion, Mater. Sci. Eng. A (2020), https://doi.org/10.1016/j.msea.2020.139746

[11] H. Zare, M. Jahedi, M.R. Toroghinejad, M. Meratian, M. Knezevic, Compressive, shear, and fracture behavior of CNT reinforced Al matrix composites manufactured by severe plastic deformation, Mater. Des. 106 (2016) 112–119, https://doi.org/10.1016/j.matdes.2016.05.109

[12] R. Casati, M. Vedani, Metal Matrix Composites Reinforced by nano-particles—a review, Metals 4 (2014) 65–83, https://doi.org/10.3390/met4010065

[13] M. Balakrishnan, I. Dinaharan, K. Kalaiselvan, R. Palanivel, Friction stir processing of Al3Ni intermetallic particulate reinforced cast aluminum matrix composites: microstructure and tensile properties, J. Mater. Res. Technol. 9 (2020) 4356–4367, https://doi.org/10.1016/j.jmrt.2020.02.060

[14] H.D. Guan, C.J. Li, P. Gao, K.G. Prashanth, J. Tan, J. Eckert, et al., Aluminum matrix composites reinforced with metallic glass particles with core-shell structure, Mater. Sci. Eng. A 771 (2020) 138630, https://doi.org/10.1016/j.msea.2019.138630

[15] Ş. Karabulut, U. Gökmen, H. Çinici, Study on the mechanical and drilling properties of AA7039 composites reinforced with Al$_2$O$_3$/B$_4$C/SiC particles, Compos. Part B Eng. 93 (2016) 43–55, https://doi.org/10.1016/j.compositesb.2016.02.054

[16] M.S. Kadam, V.D. Shinde, Stir cast aluminium metal matrix composites with mechanical and micro-structural behavior: a review, Mater. Today Proc. (2020) 845–852, https://doi.org/10.1016/j.matpr.2020.01.017

[17] A. Riquelme, P. Rodrigo, M.D. Escalera-Rodriguez, J. Rams, Effect of the process parameters in the additive manufacturing of in situ Al/AlN samples, J. Manuf. Process. 46 (2019) 271–278, https://doi.org/10.1016/j.jmapro.2019.09.011

[18] A. Lekatou, A.E. Karantzalis, A. Evangelou, V. Gousia, G. Kaptay, Z. Gácsi, et al., Aluminium reinforced by WC and TiC nanoparticles (ex-situ) and aluminide particles (*in-situ*): microstructure, wear and corrosion behaviour, Mater. Des. 65 (2015) 1121–1135, https://doi.org/10.1016/j.matdes.2014.08.040

[19] Y. Wang, M. Song, S. Ni, Y. Xue, In situ formed core–shell structured particle reinforced aluminum matrix composites, Mater. Des. 56 (2014) 405–408, https://doi.org/10.1016/j.matdes.2013.11.030

[20] H. Ghandvar, S. Farahany, T.A. Abu Bakar, A novel method to enhance the performance of an ex-situ Al/Si-YSZ metal matrix composite, J. Alloy. Compd. 823 (2020) 153673, https://doi.org/10.1016/j.jallcom.2020.153673

[21] C.J. Hsu, C.Y. Chang, P.W. Kao, N.J. Ho, C.P. Chang, Al–Al3Ti nanocomposites produced in situ by friction stir processing, Acta Mater. 54 (2006) 5241–5249, https://doi.org/10.1016/j.actamat.2006.06.054

[22] M. Yamaguchi, Y. Umakoshi, T. Yamane, Plastic deformation of the intermetallic compound Al3Ti, Philos. Mag. A 55 (1987) 301–315, https://doi.org/10.1080/01418618708209869

[23] R. Gupta, G.P. Chaudhari, B.S.S. Daniel, Strengthening mechanisms in ultrasonically processed aluminium matrix composite with *in-situ* Al3Ti by salt addition, Compos. Part B Eng. 140 (2018) 27–34, https://doi.org/10.1016/j.compositesb.2017.12.005

[24] S. Ma, X. Wang, Mechanical properties and fracture of *in-situ* Al$_3$Ti particulate reinforced A356 composites, Mater. Sci. Eng. A 754 (2019) 46–56, https://doi.org/10.1016/j.msea.2019.03.044

[25] J. Qin, G. Chen, B. Wang, N. Hu, F. Han, Z. Du, Formation of *in-situ* Al3Ti particles from globular Ti powders and Al alloy melt under ultrasonic vibration, J. Alloy. Compd. 653 (2015) 32–38, https://doi.org/10.1016/j.jallcom.2015.09.005

[26] G. Chen, X. Song, N. Hu, H. Wang, Y. Tian, Effect of initial Ti powders size on the microstructures and mechanical properties of Al3Ti/2024 Al composites prepared by ultrasonic assisted *in-situ* casting, J. Alloy. Compd. 694 (2017) 539–548, https://doi.org/10.1016/j.jallcom.2016.10.039

[27] M. Tamizi Junqani, H.R. Madaah Hosseini, A. Azarniya, Comprehensive structural and mechanical characterization of *in-situ* Al–Al3Ti nanocomposite modified by heat treatment, Mater. Sci. Eng. A 785 (2020) 139351, https://doi.org/10.1016/j.msea.2020.139351

[28] A. Rezaei, H.R.Madaah Hosseini, Evolution of microstructure and mechanical properties of Al-5wt% Ti composite fabricated by P/M and hot extrusion: effect

of heat treatment, Mater. Sci. Eng. A 689 (2017) 166–175, https://doi.org/10.1016/j.msea.2017.02.049

[29] E. Basiri Tochaee, H.R. Madaah Hosseini, S.M.Seyed Reihani, Fabrication of high strength *in-situ* Al-Al3Ti nanocomposite by mechanical alloying and hot extrusion: investigation of fracture toughness, Mater. Sci. Eng. A 658 (2016) 246–254, https://doi.org/10.1016/j.msea.2016.02.010

[30] A. Nouri, P.D. Hodgson, C.E. Wen, Effect of process control agent on the porous structure and mechanical properties of a biomedical Ti-Sn-Nb alloy produced by powder metallurgy, Acta Biomater. 6 (2010) 1630–1639, https://doi.org/10.1016/j.actbio.2009.10.005

[31] A.S. Rogachev, K.V. Kuskov, N.F. Shkodich, D.O. Moskovskikh, A.O. Orlov, A.A. Usenko, et al., Influence of high-energy ball milling on electrical resistance of Cu and Cu/Cr nanocomposite materials produced by Spark Plasma Sintering, J. Alloy. Compd. 688 (2016), https://doi.org/10.1016/j.jallcom.2016.07.061

[32] A.S. Rogachev, Mechanical activation of heterogeneous exothermic reactions in powder mixtures, Russ. Chem. Rev. 88 (2019) 875–900, https://doi.org/10.1070/RCR4884

[33] M. Abedi, D.O. Moskovskikh, A.S. Rogachev, A.S. Mukasyan, Spark plasma sintering of titanium spherical particles, Metall. Mater. Trans. B Process. Metall. Mater. Process. Sci. 47 (2016), https://doi.org/10.1007/s11663-016-0732-8

[34] D.V. Dudina, A.K. Mukherjee, Reactive spark plasma sintering: successes and challenges of nanomaterial synthesis, J. Nanomater. 2013 (2013).

[35] P.A. Loginov, S. Vorotilo, D.A. Sidorenko, Y.V. Lopatina, A. Okubayev, N.V. Shvyndina, Influence of Ti and TiH2 Additives on the structure and properties of copper alloys for diamond cutting tools, Russ. J. Non Ferr. Met. 61 (2020) 429–435, https://doi.org/10.3103/S1067821220040069

[36] E.A. Olevsky, D.V. Dudina, Field-assisted sintering, Springer International Publishing, Cham, 2018, https://doi.org/10.1007/978-3-319-76032-2

[37] C. Oses, E. Gossett, D. Hicks, F. Rose, M.J. Mehl, E. Perim, et al., AFLOW-CHULL: cloud-oriented platform for autonomous phase stability analysis, J. Chem. Inf. Model. 58 (2018) 2477–2490, https://doi.org/10.1021/acs.jcim.8b00393

[38] S.P. Ong, L. Wang, B. Kang, G. Ceder, Li–Fe–P–O 2 phase diagram from first principles calculations, Chem. Mater. 20 (2008) 1798–1807, https://doi.org/10.1021/cm702327g

[39] S.P. Ong, A. Jain, G. Hautier, B. Kang, G. Ceder, Thermal stabilities of delithiated olivine MPO4 (M=Fe, Mn) cathodes investigated using first principles calculations, Electrochem. Commun. 12 (2010) 427–430, https://doi.org/10.1016/j.elecom.2010.01.010

[40] W.D. Richards, L.J. Miara, Y. Wang, J.C. Kim, G. Ceder, Interface stability in solid-state batteries, Chem. Mater. 28 (2016) 266–273, https://doi.org/10.1021/acs.chemmater.5b04082

[41] A. Belsky, M. Hellenbrandt, V.L. Karen, P. Luksch, New developments in the inorganic crystal structure database (ICSD): accessibility in support of materials research and design, Acta Crystallogr. Sect. B Struct. Sci. 58 (2002) 364–369, https://doi.org/10.1107/S0108768102006948

[42] G. Hautier, C.C. Fischer, A. Jain, T. Mueller, G. Ceder, Finding nature's missing ternary oxide compounds using machine learning and density functional theory, Chem. Mater. 22 (2010) 3762–3767, https://doi.org/10.1021/cm100795d

[43] S.P. Ong, S. Cholia, A. Jain, M. Brafman, D. Gunter, G. Ceder, et al., The materials application programming interface (API): A simple, flexible and efficient API for materials data based on REpresentational State Transfer (REST) principles, Comput. Mater. Sci. 97 (2015) 209–215, https://doi.org/10.1016/j.commatsci.2014.10.037

[44] Z. Lu, F. Ciucci, Metal borohydrides as electrolytes for solid-state Li, Na, Mg, and Ca batteries: a first-principles study, Chem. Mater. 29 (2017) 9308–9319, https://doi.org/10.1021/acs.chemmater.7b03284

[45] W. Sun, S.T. Dacek, S.P. Ong, G. Hautier, A. Jain, W.D. Richards, et al., The thermodynamic scale of inorganic crystalline metastability, Sci. Adv. 2 (2016) e1600225, https://doi.org/10.1126/sciadv.1600225

[46] R. Folch, M. Plapp, Quantitative phase-field modeling of two-phase growth, Phys. Rev. E. 72 (2005) 011602, https://doi.org/10.1103/PhysRevE.72.011602

[47] K.G. Prashanth, Influence of mechanical activation on decomposition of titanium hydride, Mater. Manuf. Process. (2010), https://doi.org/10.1080/10426911003720870

[48] N. Thiyaneshwaran, K. Sivaprasad, B. Ravisankar, Nucleation and growth of TiAl3 intermetallic phase in diffusion bonded Ti/Al metal intermetallic laminate, Sci. Rep. (2018), https://doi.org/10.1038/s41598-018-35247-0

[49] B. Ti, Al Assari A.H., B. Eghbali, Microstructure and kinetics of intermetallic phase formation during solid state diffusion bonding in bimetal Ti/Al, Phys. Met. Metallogr. 120 (2019) 280–290, https://doi.org/10.1134/S0031918×19030025

[50] M. Romero-Romero, C. Domínguez-Ríos, R. Torres-Sánchez, A. Aguilar-Elguezabal, Core/multi-shell particles based on TiH2, a high-performance thermally activated foaming agent, Mater. Chem. Phys. 243 (2020) 122591, https://doi.org/10.1016/j.matchemphys.2019.122591

[51] C. Chirico, S. Tsipas, F. Toptan, E. Gordo, Development of Ti-Nb and Ti-Nb-Fe beta alloys from TiH 2 powders, Powder Met. 62 (2019) 44–53, https://doi.org/10.1080/00325899.2018.1563953

[52] S. Vorotilo, P.A. Loginov, D.Y. Kovalev, E.A. Levashov, DFT – Driven design of hierarchically structured, strong and highly conductive alloys in Cu-Ti system via in situ hydration - re-oxidation, J. Alloy. Compd. 832 (2020) 154823, https://doi.org/10.1016/j.jallcom.2020.154823

[53] S. Vorotilo, P.A. Loginov, A.Y. Churyumov, A.S. Prosviryakov, M.Y. Bychkova, S.I. Rupasov, et al., Manufacturing of conductive, wear-resistant nanoreinforced cu-ti alloys using partially oxidized electrolytic copper powder, Nanomaterials 10 (2020) 1261, https://doi.org/10.3390/nano10071261

[54] P. Claudy, B. Bonnetot, J.M. Letoffe, Preparation et proprietes physico-chimiques de l'hydrure d'aluminium AlH3γ, J. Therm. Anal. 15 (1979) 129–139, https://doi.org/10.1007/BF01910204

[55] C.J. Bartel, A. Trewartha, Q. Wang, A. Dunn, A. Jain, G. Ceder, A critical examination of compound stability predictions from machine-learned formation energies, Npj Comput. Mater. 6 (2020) 97, https://doi.org/10.1038/s41524-020-00362-y

[56] M. Ma, L. Liang, L. Wang, Y. Wang, Y. Cheng, B. Tang, et al., Phase transformations of titanium hydride in thermal desorption process with different heating rates, Int. J. Hydrog. Energy (2015), https://doi.org/10.1016/j.ijhydene.2015.05.083

[57] J.G. Lou, V.L. Acoff, Interfacial reactions of titanium and aluminum during diffusion welding, Weld. J. (2000).

[58] Y. Mishin, C. Herzig, Diffusion in the Ti–Al system, Acta Mater. 48 (2000) 589–623, https://doi.org/10.1016/S1359-6454(99)00400-0

[59] F.J. van Loo, G. Rieck, Diffusion in the titanium–aluminium system—II. Interdiffusion in the composition range between 25 and 100at% Ti, Acta Met. 21 (1973) 73–84, https://doi.org/10.1016/0001-6160(73)90221-6

[60] G.M. Hood, Diffusion in α-Zr, HCP and open metals, Defect Diffus. Forum 95–98 (1993) 755–774, https://doi.org/10.4028/www.scientific.net/DDF.95-98.755

[61] M. Köppers, C. Herzig, M. Friesel, Y. Mishin, Intrinsic self-diffusion and substitutional Al diffusion in α-Ti, Acta Mater. 45 (1997) 4181–4191, https://doi.org/10.1016/S1359-6454(97)00078-5

[62] U.R. Kattner, J.-C. Lin, Y.A. Chang, Thermodynamic assessment and calculation of the Ti-Al system, Metall. Trans. A 23 (1992) 2081–2090, https://doi.org/10.1007/BF02646001

[63] L. Xu, Y.Y. Cui, Y.L. Hao, R. Yang, Growth of intermetallic layer in multi-laminated Ti/Al diffusion couples, Mater. Sci. Eng. A 435–436 (2006) 638–647, https://doi.org/10.1016/j.msea.2006.07.077

[64] F.J.J.Loo Van, Diffusion in the titanium-aluminium system, Tech. Hogesch. Eindh. (1971), https://doi.org/10.6100/IR36207

[65] X. Zhang, C.-Y. Wang, First-principles study of vacancy formation and migration in clean and Re-doped γ′-Ni3Al, Acta Mater. 57 (2009) 224–231, https://doi.org/10.1016/j.actamat.2008.08.052

[66] G. Zhu, Y. Dai, D. Shu, Y. Xiao, Y. Yang, J. Wang, et al., Diffusion mechanisms of vacancy and doped Si in Al3Ti from first-principles calculations, Intermetallics 19 (2011) 1036–1040, https://doi.org/10.1016/j.intermet.2011.03.012

[67] J.R. Scully, G.A. Young, S.W. Smith, Hydrogen embrittlement of aluminum and aluminum-based alloys, Gaseous Hydrogen Embrittlement of Materials in Energy Technologies, Elsevier, 2012, pp. 707–768, https://doi.org/10.1533/9780857093899.3.707

[68] A.F. Beck, M.A. Heine, E.J. Caule, M.J. Pryor, The kinetics of the oxidation of Al in oxygen at high temperature, Corros. Sci. 7 (1967) 1–22, https://doi.org/10.1016/S0010-938X(67)80066-0

[69] T.H. Quach-Kamimura, D. David, G. Beranger, A. Falanga, G. Lozes, The mutual interactions of oxygen and hydrogen in α-titanium during heat treatment, J. Less Common Met. 125 (1986) 59–73, https://doi.org/10.1016/0022-5088(86)90080-9

[70] I.B. Ulanovskiy, Hydrogen diffusion and porosity formation in aluminium, Izdatelskiy Dom 'MISIS,' Moscow, 2015. ⟨http://eanw.info/enzilkopedia/ulanovskii/ulanovsky-hydrogen.pdf⟩.

[71] W. Eichenauer, K. Hattenbach, A. Pebler, The solubility of hydrogen in solid and liquid aluminum, Z. Met. 52 (1961) 682–684.

[72] C.E. Ransley, D.E.J. Talbot, Wasserstoff-Porosität in Metallen unter besonderer Berücksichtigung des Aluminiums und seiner Legierungen, Int. J. Mater. Res. 46 (1955) 328–337, https://doi.org/10.1515/ijmr-1955-460505

[73] W. Eichenauer, A. Pebler, Messung des diffusion und loslichkeit von wasserstoff in aluminum und kipfer, Z. Met. 48 (1957) 373–378.

[74] S. Matsuo, T. Hirata, Diffusion of Hydrogen in Aluminium, J. Jpn. Inst. Met. 31 (1967) 590–593, https://doi.org/10.2320/jinstmet1952.31.4_590

[75] K. Papp, E. Kovács-Csetényi, Diffusion of hydrogen in high purity aluminium, Scr. Metall. 15 (1981) 161–164, https://doi.org/10.1016/0036-9748(81)90321-5

[76] R.A. Outlaw, D.T. Peterson, F.A. Schmidt, Diffusion of hydrogen in pure large grain aluminum, Scr. Metall. 16 (1982) 287–292, https://doi.org/10.1016/0036-9748(82)90354-4

[77] M. Ichimura, M. Imabayashi, M. Hayakawa, Measurement of the diffusion coefficient and solubility of hydrogen in solid aluminum, J. Jpn. Inst. Met. 43 (1979) 876–883, https://doi.org/10.2320/jinstmet1952.43.9_876

[78] E. Hashimoto, T. Kino, Hydrogen diffusion in aluminium at high temperatures, J. Phys. F. Met. Phys. 13 (1983) 1157–1165, https://doi.org/10.1088/0305-4608/13/6/013

[79] T. Ishikawa, R.B. McLellan, The diffusivity of hydrogen in aluminum, Acta Metall. 34 (1986) 1091–1095, https://doi.org/10.1016/0001-6160(86)90219-1

[80] H. Saitoh, Y. Iijima, H. Tanaka, Hydrogen diffusivity in aluminium measured by a glow discharge permeation method, Acta Metall. Mater. 42 (1994) 2493–2498, https://doi.org/10.1016/0956-7151(94)90329-8

[81] V.I. Dobatkin, R.M. Gabidullin, B.A. Kolachev, G.S. Makarov, Gases and Oxides in Wrought Aluminum Alloys [in Russian], Metallurgy, Moscow, 1976.

[82] B.G. Gelman, Interaction of solid aluminium with hydrogen and water: The abstract of Ph.D. thesis in Engineering Science, 1972.

[83] E.A. Denisov, T.N. Kompaniei, A.A. Kurdiumov, The study hydrogen permeability of aluminium through the method of concentration pulses, Mater. Eng. 5 (2006).

[84] G.A. Young, J.R. Scully, The diffusion and trapping of hydrogen in high purity aluminum, Acta Mater. 46 (1998) 6337–6349, https://doi.org/10.1016/S1359-6454(98)00333-4

[85] L.A. Andreev, A.F. Viatkin, B.V. Levchuk, Kinetics of hydrogen interaction with solid aluminium, N. High. Educ. Inst. Nonferrous Ind. 5 (1975).

[86] H.R.Z. Sandim, B.V. Morante, P.A. Suzuki, Kinetics of thermal decomposition of titanium hydride powder using in situ high-temperature X-ray diffraction (HTXRD), Mater. Res. 8 (2005) 293–297, https://doi.org/10.1590/S1516-14392005000300012

[87] K.L. Firestein, S. Corthay, A.E. Steinman, A.T. Matveev, A.M. Kovalskii, I.V. Sukhorukova, et al., High-strength aluminum-based composites reinforced with BN, AlB2 and AlN particles fabricated via reactive spark plasma sintering of Al-BN powder mixtures, Mater. Sci. Eng. A 681 (2017) 1–9, https://doi.org/10.1016/j.msea.2016.11.011

[88] G. Wu, Q. Zhang, X. Yang, Z. Huang, W. Sha, Effects of particle/matrix interface and strengthening mechanisms on the mechanical properties of metal matrix composites, Compos. Interfaces 21 (2014) 415–429, https://doi.org/10.1080/15685543.2014.872914

[89] S. Vorotilo, P. Loginov, L. Mishnaevsky, D. Sidorenko, E. Levashov, Nanoengineering of metallic alloys for machining tools: multiscale computational and in situ TEM investigation of mechanisms, Mater. Sci. Eng. A. 739 (2019) 480–490, https://doi.org/10.1016/j.msea.2018.10.070

[90] M. Rahimian, N. Ehsani, N. Parvin, H. reza Baharvandi, The effect of particle size, sintering temperature and sintering time on the properties of Al-Al2O3 composites, made by powder metallurgy, J. Mater. Process. Technol. 209 (2009) 5387–5393, https://doi.org/10.1016/j.jmatprotec.2009.04.007

[91] L. Silvestroni, H.-J. Kleebe, W.G. Fahrenholtz, J. Watts, Super-strong materials for temperatures exceeding 2000 °C, Sci. Rep. 7 (2017) 40730, https://doi.org/10.1038/srep40730

[92] S. Ma, X. Wang, Mechanical properties and fracture of *in-situ* Al3Ti particulate reinforced A356 composites, Mater. Sci. Eng. A 754 (2019) 46–56, https://doi.org/10.1016/j.msea.2019.03.044